Evaluation and improvement of a cold pool parameterization against Large Eddy Simulations

Mamadou Lamine Thiam[1], Frédéric Hourdin[1], Jean-Yves Grandpeix[1], Catherine Rio[2], and Maélle Coulon–Decorzens[1]

[1]LMD/IPSL/SU/CNRS
[2]CNRM/MeteoFrance/CNRS

Correspondence: Mamadou Lamine Thiam (lamine.thiam@lmd.ipsl.fr)

Abstract. Cold pools, formed under clouds by the evaporation of precipitation, play a central role in maintaining and organizing atmospheric convection. It is suspected that their absence in climate models may lead to significant errors in the representation of convection, such as the premature convection extinction after sunset. The introduction of a cold pool parameterization into the LMDZ climate model has significantly improved the representation of convection, in particular its diurnal cycle. However, this parameterization had not yet been accurately evaluated in terms of representing the cold pool properties. This work provides for the first time such an evaluation based on Large Eddy Simulation (LES). First, we evaluate the physical relationships underlying the cold pool model in the LES, then, in a second step, its behavior when coupled with the deep convection scheme in the single-column version of LMDZ. The analyses carried out demonstrate the relevance of the assumptions underlying the parameterization. The initial version actually captures the main characteristics of LES cold pools but also exhibits some biases. We show how substantial modifications to the cold pool scheme and a readjustment of certain free parameters helped reduce those biases significantly. The remaining flaws could be corrected by adding convective mixing through thermal plumes within the cold pools and by modeling the evolution of cold pools number density rather than imposing it.

Version 23 : corrections Lamine + Jean-Yves + Catherine

1 Introduction

During thunderstorms, a significant amount of precipitation evaporates before reaching the ground, generating cold air masses in the layers below the clouds. This cooled air, denser than its surroundings, collapses and then spreads horizontally across the surface, forming so-called cold pools. These are often associated with a gust front, capable of lifting the surrounding warm air and thus promoting the development of new convective cells. In organized propagative systems such as squall lines, convective columns are permanently generated by cold pool fronts at the front of the system (Rotunno et al., 1988; Weisman and Rotunno, 2004). When the cold pool is accompanied by a gust front, it is called a density current. These density currents are fueled by precipitating downdrafts, which is their main dynamic driver. Present over both continents and oceans, density currents are

generally deeper, colder, and propagate more rapidly over continents. They play a key role in the self-aggregation of tropical convection (Jeevanjee and Romps, 2013), as well as in the transition between shallow and deep convection (Khairoutdinov and Randall, 2006; Böing et al., 2012)

In atmospheric Global Circulation Models (GCMs), as those used for climate change studies, convection has to be parameterized due to the coarse horizontal resolution (30 to 300 km). Simulating convective rainfall with parameterized physics is challenging (Randall et al., 2003). GCMs often underestimate rainfall rates (Kendon et al., 2012; Pantillon et al., 2015; Tan et al., 2018) and produce peak precipitation at noon, in phase with insolation, while the maximum precipitation is generally observed in late afternoon or during night (Randall et al., 2003; Guichard et al., 2004; Stephens et al., 2010; Dirmeyer et al., 2012). Density currents probably play a key role in this timing, by self-maintaining convection (Pantillon et al., 2015; Grant et al., 2018). One of the first attempts to parameterize density currents was proposed by Qian et al. (1998). Later on, Grandpeix and Lafore (2010) proposed a parameterization based on a population of identical circular density currents that are cooled by convective precipitation. The coupling of the Emanuel (1991) parameterization of deep convection with this cold pool parameterization and with the thermal plume model of Rio and Hourdin (2008) in the LMDZ climate model significantly improved the simulation of the diurnal cycle of precipitation in the tropics (Rio et al., 2009), shifting its maximum from noon to mid afternoon. A further improvement was brought by the introduction of the stochastic triggering of deep convection (Rochetin et al., 2014) which made the simulated convection more intermittent. Despite this success, and the use of the cold pool model in the standard version of the LMDZ atmospheric and IPSL (Institut Pierre Simon Laplace) coupled models (Hourdin et al., 2020; Boucher et al., 2020), it was not evaluated in details so far. At the same time, other parameterizations have been develop to include the impact of cold pools on convection, but without necessarily evaluating in details simulated cold pool characteristics and properties (Park, 2014; Del Genio et al., 2015). This is explained not only by a lack of observational data but also by the fact that the internal variables of parameterizations are not directly accessible from observations.

Large Eddy Simulations (LES) are a useful complement to observations. Their fine horizontal resolution enables them to simulate explicitly turbulent and convective motions in the boundary layer (Brown et al., 2002; Siebesma et al., 2003). One advantage of LES compared to observations is that they provide full three-dimensional information. They have been used extensively to develop and evaluate boundary layer and convection parameterizations (Rio et al., 2010; Dorrestijn et al., 2013; Strauss et al., 2019; Legay et al., 2025). LES have been used to simulate and understand cold pools (Feng et al., 2015; Meyer and Haerter, 2020; Lochbihler et al., 2021), as well as to develop parameterizations of cold pools (Kurowski et al., 2018). However, their use for a cold pool parameterization assessment remains unexplored.

Here we propose to use LES to evaluate in details the parameterization of cold pools of LMDZ (Grandpeix and Lafore, 2010; Grandpeix et al., 2010). We first use LES to evaluate some of the fundamental relationships between large scale state variables (for LES, the horizontal average over the domain) and internal variables which are at the basis of the parameterization. We then propose improvements which are further assessed in simulations with a Single-Column-Model (SCM) version of LMDZ against LES. In such simulations, the parameterization interacts with all the other parameterizations and depend on the values of a number of free parameters. To explore the sensitivity of the results to those free parameters and retune the model after improvement of its physical content, we use a tool for automatic calibration, High-Tune-Explorer, developed recently

(Couvreux et al., 2021; Hourdin et al., 2021). This tool, based on history matching, can be used to characterize the subspace of parameter values for which the model is in agreement with LES, given a series of target metrics and associated tolerance to error (Couvreux et al., 2021). It is used here to explore the sensitivity of the agreement between SCM simulations and LES to the model free parameters.

The paper starts by presenting in section 1 the tools used: the LMDZ model, the cold pool parameterization by Grandpeix and Lafore (2010) (referred to as the GL10 hereafter), and the LES used for evaluation. The presentation of the tuning tool (largely published) and the setup of its use is let to an appendix to concentrate on model physics and improvement in the core of the paper. In section 2, we detail the cold pool sampling in LES, designed to assess the physical laws internal to the cold pool parameterization and its coupling with deep convection. Section 3 is devoted to a comparison of cold pool model variables simulated by LMDZ in SCM mode and those calculated in LES, in order to identify the model's limitations. These results will then be discussed, and proposed improvements will be detailed in section 4. Finally, we conclude with a synthesis and discussion of prospects in section 5.

2 Tools and methods

2.1 LMDZ and its single-column version

LMDZ is the General Circulation Model (GCM) used in this work. Developed in the 1970s at Laboratoire de Meteorologie Dynamique (Sadourny, 1984; Hourdin et al., 2006). It is based on simplified Navier-Stokes equations for fluid mechanics, as well as transport equations. It represents the second generation (Hourdin et al., 2013) of a climate model initially described by Sadourny and Laval (1984). LMDZ is the atmospheric component of the IPSL coupled model. The latter is one of around twenty coupled models taking part in major international model intercomparison exercises, such as those of the CMIP (Coupled Model Intercomparison Project), the results of which are used in IPCC (Intergovernmental Panel on Climate Change) reports. We use here the LMDZ6A configuration of LMDZ designed for CMIP6 and described by Hourdin et al. (2020).

LMDZ consists of two main parts, from a physical, mathematical and computational point of view. The first part, called "the dynamics", concerns the numerical resolution of the atmospheric general circulation equations. This component manages horizontal exchanges between the model's grid cells. The second part, called "physics", calculates the impact of radiation, small-scale processes (subgrid) and phase changes of water on dynamic variables via "physical parameterizations". This "physical" part is made up of juxtaposed atmospheric columns, which do not interact with each other. Within each column, the variables are assumed to be statistically homogeneous in the horizontal plane.

The SCM version of LMDZ is built by extracting an atmospheric column from the GCM, incorporating all subgrid-scale parameterizations, and running it in a large-scale constrained environment. This approach has become central in the development and tuning of parameterizations of convection and associated clouds in several climate modeling groups (Zhang et al., 2016; Gettelman et al., 2019). Parameterizations are often developed and evaluated within this single-column framework by comparing them with LES of the same atmospheric column. The SCM/LES approach was promoted in particular by GCSS (GEWEX Cloud Systems Study), a program aimed at improving the parameterization of cloud systems in climate models (Krueger et al.,

2016). A major advantage of the SCM is its low computational cost, which allows a large number of simulations, even on a laptop, making it particularly useful in the development phase, where extensive testing is required.

2.2 Convective parameterizations in LMDZ

The role of convective parameterizations is to provide sources of heating Q_1 and moistening Q_2 to the conservation equations of potential temperature θ and specific humidity qv :

$$C_p \frac{D\theta}{Dt} = Q_R + (L_v + f_g L_f)(c-e) - C_p \frac{1}{\rho}\frac{\partial \rho \overline{w'\theta'}}{\partial z} \quad = Q_R + Q_1 \tag{1}$$

$$\frac{Dqv}{Dt} = e - c - \frac{1}{\rho}\frac{\partial \rho \overline{w'qv'}}{\partial z} \quad = -Q_2/L_v \tag{2}$$

where C_p is the heat capacity of dry air, Q_R is the radiative heating, c and e are condensation and evaporation rates, f_g is the condensate ice fraction, L_v is the latent heat of vaporization and L_f the latent heat of fusion. For any state variable ϕ, the source term should include the vertical convergence of the Reynolds turbulent flux of the quantity $-\partial_z \rho \overline{w'\phi'}/\rho$, representing the effect of subgrid-scale turbulent or convective motions on the explicitly resolved large scale flow. The convective parameterizations also often provide a source term Q_3 for momentum but it is not involved in the coupling with cold pools described here.

Note that the equations above are simplified assuming that the ice fraction f_g is unchanged by evaporation and condensation. Note also that Q_2 is a sink of humidity expressed conventionally as a heating term with constant L_v.

The parameterization of turbulence, convection and clouds in LMDZ is based on a multi-scale, or object view.

2.2.1 The small scale turbulence,

mainly active near the surface, is accounted for following Yamada (1983) scheme, with an eddy diffusive approach in which the eddy diffusivity relies on a prognostic equation for the turbulent kinetic energy.

2.2.2 The thermal plume model

was developed specifically to account for the vertical transport by organised thermal plumes, cells or rolls in the convective boundary layer (Hourdin et al., 2002; Rio and Hourdin, 2008). The population of convective structures within a grid cell are summarized into a mean ascending plume, with a unique ascending mass flux $f_{th} = \rho \alpha_{th} w_{th}$, compensated by a mass flux $-f_{th}$ in a fraction $1 - \alpha_{th}$ of the grid cell. The sources ${Q_1}^{\text{th}}$ and ${Q_2}^{\text{th}}$ only contain the vertical convergence of the mass flux transport ($\rho \overline{w'\phi'} = f_{th}(\phi_{th} - \phi)$ where ϕ_{th} is the value of variable ϕ within the thermal plume), the part coming from the condensation or evaporation being treated in the so-called large-scale condensation scheme.

2.2.3 The large-scale condensation scheme

is used to predict the cloud fraction except for deep convection, based on a probability distribution function (PDF) of the total water within the horizontal grid cell (giving the cloud fraction as the part of the grid cell with humidity above saturation). This statistical cloud scheme provides to first order: ${Q_1}^{\text{lsc}} = (L_v + f_g L_f)(c-e)$ and ${Q_2}^{\text{lsc}} = -L_v(c-e)$. For shallow cumulus

or strato-cumulus, cloud condensation is thus treated outside the thermal plume scheme. Both schemes are however coupled together when the thermal plume is active within a grid cell. In this case, the subgrid water PDF is prescribed as a bimodal function, with one mode corresponding to the thermal plume and the other one to its environment. This coupling led to a strong improvement in the representation of cumulus and stratocumulus clouds (Jam et al., 2013; Hourdin et al., 2019).

2.2.4 Deep convection

is represented with a modified version of the Emanuel (1991) scheme. As for shallow convection, the parameterization of deep convection represents a population of cumulonimbus clouds that would occur in the grid cell as an effective cumulonimbus cloud. However, for deep convection, the transport, condensation, cloud formation and rainfall are treated within the same scheme.

Convective transport in these cumulonimbus clouds is represented by mass fluxes and an air exchange matrix. Several "compartments" can be distinguished. **An undiluted updraft** that does not entrain air laterally above the base of the cloud, but is gradually "shed" or "eroded" while rising. It is assumed to be fast enough to carry the liquid or solid water condensed within it. Following the Episodic Mixing and Buoyancy Sorting approach, **a population of diluted ascending or descending air masses, saturated,** created by mixing a fraction of air shed from the adiabatic ascent with ambient air according to an imposed PDF. It is divided into bins defining a population of air parcels that are lofted to their neutral buoyancy level (layer), thus creating a matrix in which each term is an exchange of air between two layers of the model. Before forming these mixtures, the water in excess in the air shed from the adiabatic updraft is precipitated, and then again, the excess water is precipitated before the diluted updraft is detrained into the environment (there is no further precipitation from diluted downdrafts). Finally **the unsaturated downdrafts** receive all the rain formed during shedding or detraining in the environment. Some of these descents take place outside the clouds, in air that is not saturated with moisture, allowing them to evaporate. This evaporation of very large quantities of rain forces strong downdrafts. Below the base of the clouds, all of the precipitation is outside the clouds. Their re-evaporation is the source of density currents, or cold pools, created under cumulonimbus clouds.

In practice, the convective tendencies Q_1 and Q_2 are separated into two parts, "saturated" and "unsaturated". The saturated tendencies ${Q_1}^{\text{sat}}$ and ${Q_2}^{\text{sat}}$ take into account adiabatic updraft, diluted updrafts and downdrafts, and a downward flux in the environment compensating all these mass fluxes. The unsaturated tendencies ${Q_1}^{\text{unsat}}$ and ${Q_2}^{\text{unsat}}$ take into account unsaturated downdraft as well as compensating ascent.

The main modification of the deep convection scheme concerns the mixing formulation (Grandpeix et al., 2004) and the triggering and closure formulations (Rio et al., 2009; Rochetin et al., 2014) modified so that deep convection is controlled by sub-cloud processes: boundary-layer thermals (Rio et al., 2010) and cold pools (Grandpeix and Lafore, 2010). The cold pool scheme and the control of convection by sub-cloud processes, particularly the role of cold pools, will be detailed in the following sections.

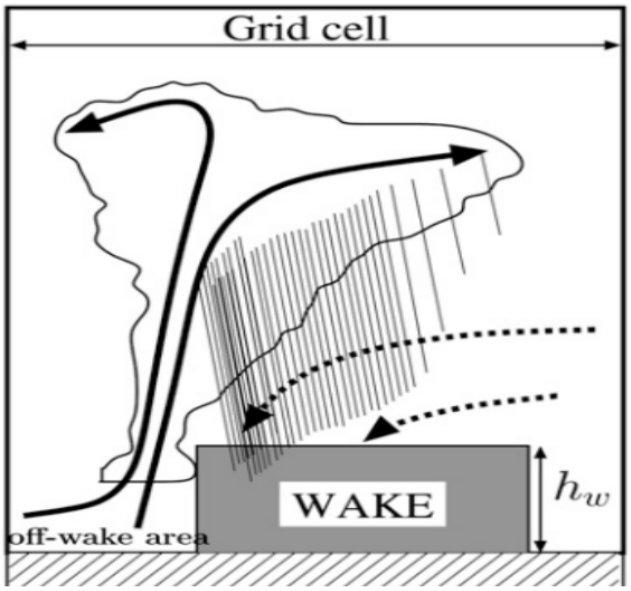

Figure 1. Conceptual diagram of a density current (Grandpeix and Lafore, 2010).

2.3 The cold pool model

The cold pool model has been entirely described in GL10. Here, we introduce the main equations and internal variables of the parameterization relevant for the rest of the paper. The cold pool model represents a population of identical circular cold pools (or wakes) over an infinite plane containing the grid cell. All the wakes have the same height, radius, and vertical profiles of thermodynamic variables. Their centers are statistically distributed with a uniform density $D_{\rm wk}$. Cold pools divide the space into two parts: (i) the interior of cold pools (w) is where convective precipitating downdrafts fall; in these downdrafts, the re-evaporation of precipitation generates intense cooling and strong negative buoyancy; (ii) the exterior of cold pools (x) contains the warm air that fuels the saturated convective currents (Fig. 1). The top height of the cold pool is defined as the altitude $h_{\rm wk}$ (and associated pressure $p_{\rm wk}$) where the temperature difference between (w) and (x) becomes zero. Below this level cold pools are cooler than their exterior: they collapse and spread out as they are denser than the surrounding air. The boundary between the cold pool and the environment is considered to be infinitely thin, and at each point on this boundary, the cold pool spreads at a rate C. C is considered to be a random variable whose mean C_* will give the rate at which the cold pool spreads. In the GL10 model, C_* scales with the square root of the potential energy available in the cold pools, i.e the cold pool's collapse energy, $WAPE$ (Wake Available Potential Energy), given by:

$$WAPE = g \int \frac{\delta\rho}{\overline{\rho}} = -g \int_0^{h_{\rm wk}} \frac{\delta\theta_v}{\overline{\theta_v}} dz \tag{3}$$

so that:

$$C_* = k\sqrt{2WAPE} \tag{4}$$

where ρ is the air density; θ_v is the virtual potential temperature.

For any variable X, $\delta X = X_{\text{wk}} - X_{\text{ex}}$ is the difference of its mean value in the two subdomains and $\overline{X}$ the average over the horizontal domain.

Coefficient k in equation (4) should take a value between 0 and 1. This coefficient should probably depend on the structure of cold pools. Based on 3D CRM (Cloud Resolving Models) simulations, Lafore (2000) estimated this coefficient to 0.33 in the case of a linear structure such as squall line. This is the value retained in LMDZ6A.

The spread rate of cold pools C_* is deduced from the following relationship:

$$\partial_t \sigma_{\text{wk}} = 2\pi r C_* D_{\text{wk}} = 2C_* \sqrt{\pi D_{\text{wk}} \sigma_{\text{wk}}} \tag{5}$$

where σ_{wk} is the surface fraction covered by cold pools (σ_{wk} = $D_{\text{wk}}\pi r^2$). Due to the complex life cycle of cold pools (including birth, death, collisions and mergers), calculating their number density requires an other parameterization. So far, the value of the cold pool number density is thus imposed. In LMDZ6A, this density is fixed to a different value over ocean (10 cold pools over 100 km$\times$100 km) and over the continent (8 cold pools over 1000 km$\times$1000 km). In the GL10 model, cold pools initially appear with a surface fraction of 2% and evolve over time according to equation 5. The evolution of σ_{wk} is arbitrarily limited to a maximum of 40% ($\sigma_{\text{wk}} \leq 0.4$). Those thresholds are one limitation of the scheme that we hope to remove in the future.

It is assumed that below the top of cold pool (p_{wk}), the vertical velocity profile associated with the subsidence of the cold pool results solely from the spreading at the surface, without lateral entrainment ($e_{\text{wk}} = 0$) or detrainment ($d_{\text{wk}} = 0$) between the cold pool and its environment. Above this level, the subsidence induces a lateral convergence of air feeding the cold pool which can be reinforced by additional reevaporation of rainfall below stratiform clouds. The shape of the vertical profile of the velocity difference $\delta\omega$ between the cold pool region and its environment is imposed as a piecewise linear function of pressure: $\delta\omega$ increases linearly from zero at the surface up to a maximum value at p_{wk} and then decreases linearly between p_{wk} and a minimum pressure p_{upper} corresponding to the upper bound of the cold pool model. The vertical subsidence which thus increases downward between p_{upper} and p_{wk} is fed by lateral entrainment

$$e_{\text{wk}} = \sigma_{\text{wk}}(1 - \sigma_{\text{wk}})\partial_p \delta\omega + \partial_t \sigma_{\text{wk}} \tag{6}$$

without detrainment. This lateral entrainment accounts for the horizontal component of the meso-scale circulation known to entrain air from low- or mid- tropospheric air into the cold pool.

At p_{upper}, the top of the cold pool model, δ_X cancels for all cold pool state variables. In GL10 model and in LMDZ6A, p_{upper} was set to 600 hPa and there was also a nonzero velocity difference ($\delta\omega^{cv}$) at p_{upper}, accounting for the difference of the convective mass fluxes between (w) and (x). In the version used in this paper, this difference is now zero ($\delta\omega^{cv} = 0$) above this level.

The cold pools contribute to the physics tendencies for temperature and humidity. It is the convective scheme which accounts for cooling in the cold pools so that no phase change is associated with the cold pool model. The source terms therefore only contain the vertical convergence of the Reynolds flux associated with mass flux transport (downward in the cold pool and upward in its environment) that reads $\rho\overline{w'\phi'} = 1/g\sigma_{\rm wk} * (1-\sigma_{\rm wk})\delta\omega\delta\phi$ for any conserved variable ϕ so that:

$$\begin{cases} {Q_1}^{\rm wk} = -C_p\ \sigma_{\rm wk}\ (1-\sigma_{\rm wk})\ \partial_p(\delta\omega\delta\theta) \\ {Q_2}^{\rm wk} = L_v\ \sigma_{\rm wk}\ (1-\sigma_{\rm wk})\ \partial_p(\delta\omega\delta qv) \end{cases} \tag{7}$$

It is the re-evaporation of rain in unsaturated downdrafts that is the primary driver of cold pool development. This process is reflected in the model by assigning the heating term ${Q_1}^{\rm unsat}$ to the interior of cold pools, while ${Q_1}^{\rm sat}$ acts on their environment. Consistent with this splitting, we assume that the saturated part of the convective scheme sees the profiles outside the cold pools, and the unsaturated downdrafts their interior. We further assume that thermal plumes are only active in the fraction of the horizontal surface located outside the cold pools. Thus the mass flux transport scheme is applied to any variable outside the cold pool $\phi_{\rm ex} = \phi - \sigma_{\rm wk}\delta\phi$, and finally ${Q_1}^{\rm th} = -C_p(1-\sigma_{\rm wk})\partial_z\rho\overline{w'\theta'_{\rm ex}}$ and ${Q_2}^{\rm th} = L_v(1-\sigma_{\rm wk})\partial_z\rho\overline{w'qv'_{\rm ex}}$. The thermal plume model therefore induces a differential tendency that is opposite of the average tendency restricted to the environment. Ultimately, the contrast in convective tendencies (shallow and deep) between the cold pools and their environment reads:

$$\begin{cases} \delta{Q_1}^{\rm cv} = \frac{{Q_1}^{\rm unsat}}{\sigma_{\rm wk}} - \frac{{Q_1}^{\rm sat}}{1-\sigma_{\rm wk}} - \frac{{Q_1}^{\rm th}}{1-\sigma_{\rm wk}} \\ \delta{Q_2}^{\rm cv} = \frac{{Q_2}^{\rm unsat}}{\sigma_{\rm wk}} - \frac{{Q_2}^{\rm sat}}{1-\sigma_{\rm wk}} - \frac{{Q_2}^{\rm th}}{1-\sigma_{\rm wk}} \end{cases} \tag{8}$$

It is the terms $\delta{Q_1}^{\rm cv}$ and $\delta{Q_2}^{\rm cv}$ that drive the time evolution of $\delta\theta$ and δq given by:

$$\begin{cases} \partial_t\delta\theta = \frac{\delta{Q_1}^{\rm cv} + \delta{Q_1}^{\rm wk}}{C_p} - \overline{\omega}\partial_p\delta\theta - \frac{K_{gw}}{\tau_{gw}}\delta\theta, \\ \\ \partial_t\delta q = -\frac{\delta{Q_2}^{\rm cv} + \delta{Q_2}^{\rm wk}}{L_v} - \overline{\omega}\partial_p\delta q \end{cases} \tag{9}$$

This time evolutions also includes a differential heating and moistening induced by the cold pools itself of the air inside and outside the cold pools, under the effect of lateral air entrainment from the environment above $p_{\rm wk}$, subsidence inside the cold pools, and compensating ascendance in the environment:

$$\begin{cases} \frac{\delta{Q_1}^{\rm wk}}{C_p} = -\frac{e_{\rm wk}}{\sigma_{\rm wk}}\delta\theta - \delta\omega\partial_p\overline{\theta} - (1-2\sigma_{\rm wk})\delta\omega\partial_p\delta\theta \\ -\frac{\delta{Q_2}^{\rm wk}}{L_v} = -\frac{e_{\rm wk}}{\sigma_{\rm wk}}\delta q - \delta\omega\partial_p\overline{q} - (1-2\sigma_{\rm wk})\delta\omega\partial_p\delta q \end{cases} \tag{10}$$

The terms $-\overline{\omega}\partial_p\delta$ in (9) partially compensate for the fact that the contrasts δ are not transported by the dynamics until now. We therefore take into account, in the parameterizations, the vertical part of large-scale advection to partially compensate for this deficiency.

Finally, the last term, present only in the θ part of (9), corresponds to the reduction in temperature contrasts by gravity waves with a coefficient specified as the ratio of an efficiency K_{gw} to a characteristic time

$$\tau_{gw} = \frac{\sqrt{\sqrt{\sigma_{\rm wk}} - (1-\sqrt{\sigma_{\rm wk}})}}{4Nz\sqrt{D_{\rm wk}}} \tag{11}$$

estimated as the time required for a wave with speed Nz (where N is the Brunt-Väisälä frequency and z is altitude) to travel a distance equal to the geometric mean of the cold pool size and the interval between cold pools

The cold pool model is now fully described. It includes:

- three prognostic variables, derived directly from the model equations: the profiles of $\delta\theta$ and δq and σ_{wk}.
- three diagnostic variables, evaluated from the profile of $\delta\theta$: p_{wk}, C_* and $WAPE$
- three main free parameters: the coefficient k, the density D_{wk} and τ_{gw}.

2.4 Triggering and closure of the deep convection scheme

Triggering and closure formulations in LMDZ have been described in Rio et al. (2013). Deep convection is triggered when the Available Lifting Energy (ALE) at cloud base exceeds the convective inhibition (CIN) threshold. This can be caused either by uplift energy from the convective boundary layer (ALE_{bl}), provided by the thermals model (Rio and Hourdin, 2008), or by energy generated by cold pools (ALE_{wk}):

$$\max(ALE_{\text{bl}}, ALE_{\text{wk}}) > |CIN| \tag{12}$$

The intensity of the convection depends on the mass flux (M_b) at the cloud base, determined from the available lifting power ALP, provided by thermals (ALP_{bl}) and cold pools (ALP_{wk}).

$$M_b = \frac{ALP_{\text{bl}} + ALP_{\text{wk}}}{(2W_b^2 + |CIN|)} \tag{13}$$

where

$$W_b = wb_{\text{srf}} + \frac{wb_{\text{max}}}{1 + \frac{\Delta P}{(P_s - P_{LFC})}} \tag{14}$$

is the vertical velocity at the level of free convection (LFC), $\Delta P = 500$ hPa and wb_{srf} and wb_{max} are model free parameters.

Concerning the boundary layer, the available lifting energy is taken as the maximum kinetic energy in the thermal plume below cloud base

$$ALE_{\text{bl}} = \frac{1}{2}{w_{th,max}}^2 \tag{15}$$

A notable improvement was introduced by Rochetin et al. (2014), with the implementation of a statistical representation of the size distribution of cloudy thermal bases. In the new statistical triggering, deep convection is activated if both $ALE_{th} > |CIN|$ and at least one cumulus cloud within a grid cell exceeds a given size, specified by S_{trig} (adjustable parameter). The available lifting power scales with ${w_{th,max}}^3$.

To calculate ALE_{wk}, the model assumes that the maximum speed (C_{max}) on the cold pool contour will trigger convection. This is assumed to be proportional to the square root of $WAPE$, with a higher coefficient of proportionality than the one used

for C_* leading to the following relationship:

$$C_{\max} = k'\sqrt{2WAPE} \tag{16}$$

where k'=1.

The Available Lifting Energy associated with cold pools is thus expressed by the following relationship:

$$ALE_{\text{wk}} = \frac{1}{2}C_{\max}^2 \tag{17}$$

Combining equations (17) and (16), one obtains:

$$ALE_{\text{wk}} = k'^2 WAPE \tag{18}$$

with $k' = 1$, meaning that, in the cold pool model, the Available Lifting Energy associated with cold pools is equal to the collapse energy.

Each cold pool generates its own lifting power, depending on its spreading speed (C_*), height (h_{wk}) and the length (L_g) of its gust front. The total power (ALP_{wk}) of the cold pools is the product of the power supplied by each pool times the cold pool number density (D_{wk}).

$$ALP_{\text{wk}} = \epsilon\frac{1}{2}\rho C_*^3 h_{\text{wk}} L_g D_{\text{wk}} \tag{19}$$

where ϵ = 0.25 is the lifting efficiency. This value means that 25% of the power associated with cold pool spreading is available for deep convection.

$$L_g = 2\pi r \tag{20}$$

$$\sigma_{\text{wk}} = D_{\text{wk}}\pi r^2 \tag{21}$$

Then, the lifting power ALP_{wk} reads:

$$ALP_{\text{wk}} = \epsilon\rho {C_*}^3 h_{\text{wk}}\sqrt{\sigma_{\text{wk}} D_{\text{wk}}\pi} \tag{22}$$

2.5 Large Eddy Simulations

Atmospheric Large Eddy Simulations (LES) are performed with non hydrostatic models, with a grid resolution fine enough to resolve the main structures (large eddies) that dominate the turbulent or convective transport. They have been widely used to study the convective boundary layer with grid resolutions of a few tens of meters (Brown et al., 2002; Siebesma et al., 2003). In the presence of water phase changes, however, these simulations can become more dependent on the microphysical

schemes used. One of the major strengths of LES lies in its ability to provide three-dimensional information not available from observations, making them an indispensable complement to the latter for understanding processes. In addition, LES can be used to validate the internal variables of parameterizations, enabling their physical realism to be assessed.

In this study, we use the outputs of two oceanic LES and one continental LES.

Both oceanic LES were carried out in Radiative-Convective Equilibrium (RCE) mode. RCE is a concept in which equilibrium is achieved between convective heating and radiative cooling of the atmosphere. A detailed description of RCE simulation protocols is provided in Daleu et al. (2015). In the RCE simulations used here, radiative computation is replaced by a constant cooling of -1.5 K per day, while the surface temperature is imposed. The destabilization leads to convection. The associated heating rate, largely corresponding to the release of latent heat by cloud condensation in convective towers, compensates for the cooling once quasi-equilibrium has been reached. Two oceanic LES of this RCE are used here, one is performed with the SAM model (Khairoutdinov and Randall, 2003) and the other one with MesoNH (Lac et al., 2018). Both simulations cover an oceanic domain of 200 km$\times$200 km with horizontal resolution of 250 m. The lateral boundary conditions are cyclic for both models. The sea surface temperature is set to 300 K. These two RCE simulations run for 44 days, with quasi steady-state regime reached after about 40 days. Output are available every 3 hours for SAM and every 24 hours for MesoNH.

The continental LES is based on the AMMA (African Monsoon Multidisciplinary Analysis) case. This case is derived from observations made on July 10, 2006 during the AMMA field campaign (Redelsperger et al., 2006), during which a relatively small, short-lived convective system formed over Niamey (Lothon et al., 2011). This system, with a lifetime of around 6 hours, was observed by various instruments (radar and atmospheric soundings), supplemented by satellite data. This case study represents a typical example of deep convection in the Sahel region (Couvreux et al., 2012). LES for this continental case is carried out with the MesoNH model over a 200 km $\times$ 200 km domain, with a horizontal resolution of 200 m. Lateral boundary conditions are cyclic and surface fluxes are imposed. Outputs are generated at a frequency of 30 minutes.

3 Assessment of the cold pool model internal equations from LES

3.1 Distinguishing the cold pools from their environment

In order to use LES for the assessment of the cold pool parameterization, the first challenge is to separate cold pools from their environment. Indeed, there is no a priori established framework for objectively identifying cold pools in observations and numerical models (Rochetin et al., 2021), and choices may depend in part on the physical picture one has of cold pools, and also, for the purpose at hand, on the picture underlying the parameterization. The first method for identifying cold pools proposed by Young et al. (1995) was based on surface precipitation rates. In more recent studies, such as those by Provod et al. (2016); Zuidema et al. (2017); Vogel et al. (2021); Rochetin et al. (2021); Touzé-Peiffer et al. (2022), the detection of cold pools is closer to a density current oriented detection, in which variations in temperature, pressure and wind are taken into account.

In the present study, the aim is not to isolate individual “cold pools objects”, but only to know whether a grid cell of the LES is inside or outside cold pools. Also the boundary conditions are idealized targeting the statistical homogeneity assumption

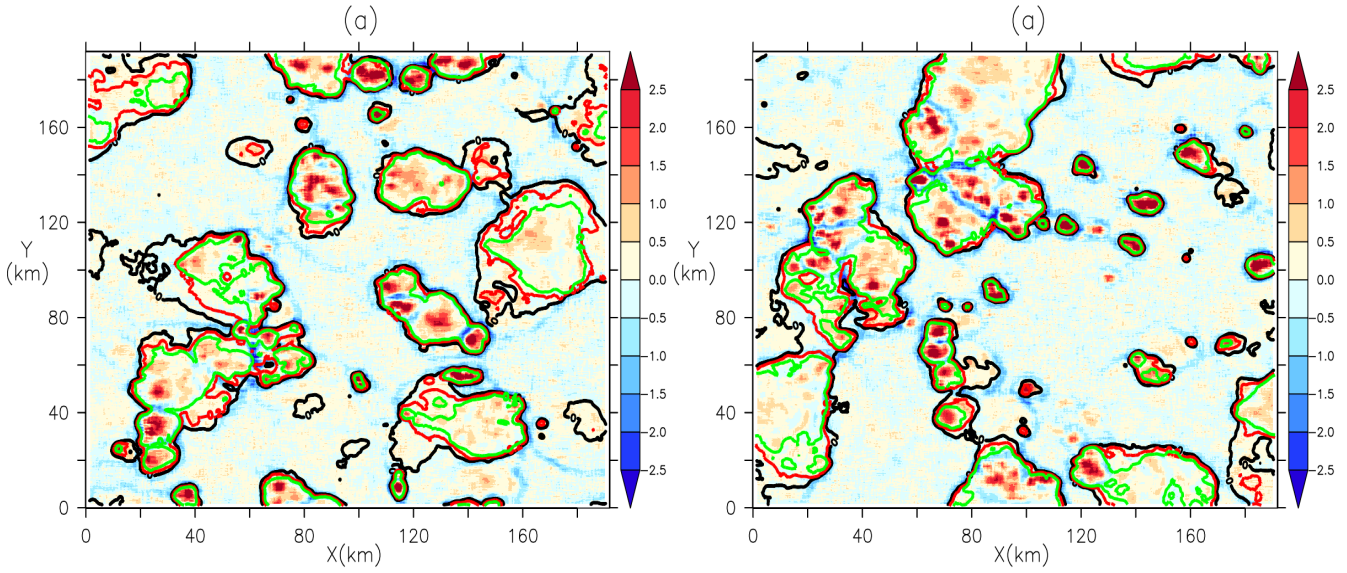

Figure 2. Moving average (with a box of 3.25 km $\times$ 3.25 km) of the divergence of wind at 10 m (in unit $10^{-3}s^{-1}$ or 1 m/s/km). Panels a and b correspond to two different states of the LES SAM carried out on the oceanic RCE case. Contours of temperature anomalies at 10 m at -0.4 K (green), -0.2 K (red) and 0 K (black) are superimposed on the smoothed divergence field.

that is at the basis of the Reynolds decomposition between dynamical core and physics parameterizations. In this idealized case with uniform surface temperature, cold pools can be identified fairly immediately using a threshold on the anomaly (after removing the domain average) of temperature at 10 m above surface, $T_{10\mathrm{m}}$, i.e. at the first model mid layer.

Fig. 2 and 3 show a horizontal moving average with a box of 3.25 km$\times$3.25 km of the divergence of the wind at 10 m above surface, $\overrightarrow{V_{10\mathrm{m}}}$. From these maps, the centers and gust fronts of cold pools can be easily identified, corresponding respectively to the maximum and minimum of divergence values. Maxima of divergence of surface wind indicate the center of cold pools where cold air masses collapse. Precipitation is generally co-located with these divergence maxima (not shown). The fairly strong wind convergence observed around cold pools centers corresponds to the strong lift of air masses created upstream of the gust front at the cold pool's periphery.

Both the two LES of the RCE case and the LES of the AMMA case show cold pools clusters forming a common gust front. This can be explained by the fact that, during propagation, cold pools can merge to create a single, larger cold pool. We can also observe that wind convergence (and thus associated updrafts) is more intense where cold pools meet. This is in line with some studies that indicate that convection initiation on gust fronts is more efficient when two or more cold pools collide (Meyer and Haerter, 2020; Torri and Kuang, 2019; Haerter and Schlemmer, 2018; Feng et al., 2015).

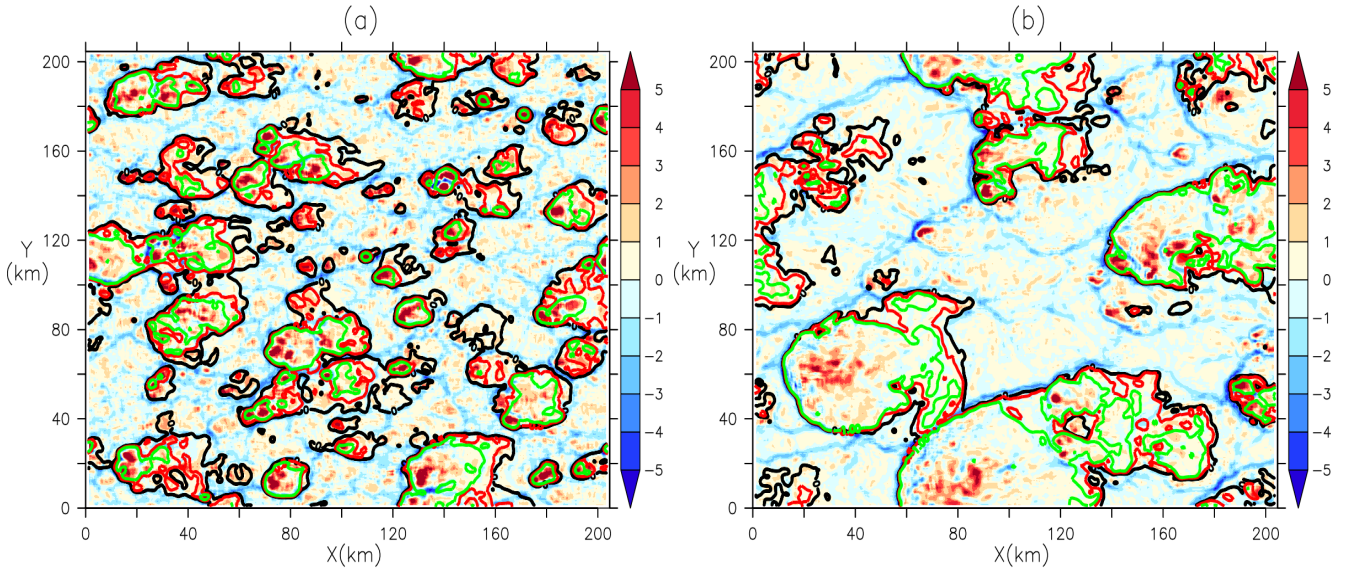

Figure 3. Same as Fig. 2 for two successive instants, 5:30 PM (a) and 7:30 PM (b), of the LES MESONH carried out on the AMMA case. The contours superimposed corresponds to $T_{10\mathrm{m}}$ anomalies of -1 K (green), -0.5 K (red) and 0 K (black).

We superimpose on this map the $T_{10\mathrm{m}}$ anomaly contours with different values to determine an optimal threshold for this anomaly. In the RCE case, the $T_{10\mathrm{m}}$ anomaly at 0 K sometimes includes regions without cold pools centers, where divergence of surface wind is low (Fig. 2a and b) while anomaly contours at -0.2 K and -0.4 K surround the centers of cold pools quite well. In the AMMA case, figure 3a clearly shows that the 0 K threshold is too high to identify cold pools. Fig. 3b, on the other hand, shows that the -1 K threshold follows gust fronts of cold pools better than the -0.5 K threshold. On the basis of these analyses, we retain the $T_{10\mathrm{m}}$ anomaly thresholds at -0.2 K and -1 K to identify cold pools in the RCE and AMMA cases respectively.

3.2 Computing the WAPE from the cold pool anomalies

Once the threshold value is fixed for the $T_{10\mathrm{m}}$ anomaly, we separate the full 3-dimensional LES domain between cold pool region (wk) and the rest of the domain (ex) form which we can compute the horizontal averages on each subdomain, X_{wk} inside cold pools and X_{ex} outside, and then the cold pool anomaly $\delta X = X_{\mathrm{wk}} - X_{\mathrm{ex}}$. This sampling allows to compute the vertical profiles of cold pools anomaly for temperature (δT), humidity (δq) and vertical velocity (δw). Examples of temperature anomalies are shown in Fig. 4.

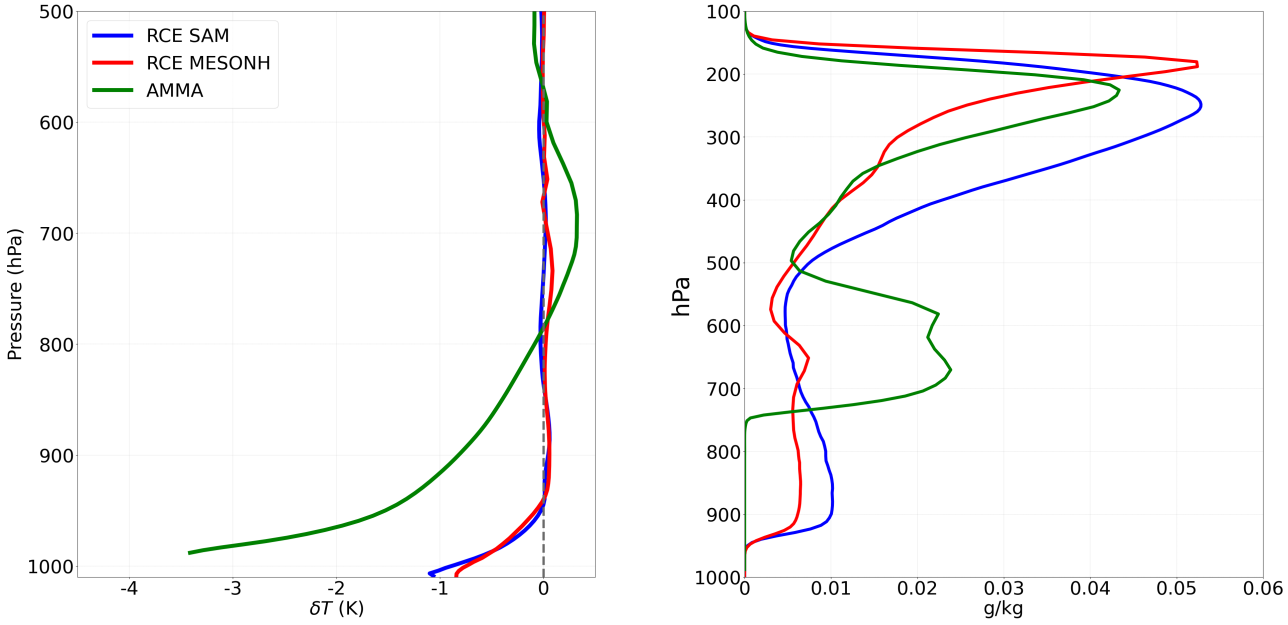

Figure 4. Vertical profiles of the cold pool temperature anomaly (left, difference between the inside and the outside of cold pools) and of the averaged condensed water (right, g/kg).

Note that we apply the same surface mask to the entire column to determine the vertical profiles. This simple vision of vertical cylinders is adopted to match the view underlying the parameterization but may be put into question in the presence of strongly tilted convection.

One can then compute the collapse energy ($WAPE$) of cold pools in the LES by integrating from the surface up to $p_{\rm wk}$, the virtual temperature anomaly, $\delta\theta_v$ (equation, 3). As suggested by Grandpeix et al. (2010), we take for $p_{\rm wk}$ the pressure where the δT profile cancels out. This altitude is around 950 hPa (approximately 600 m) in the oceanic RCE case and around 800 hPa (approximately 2 km) in the AMMA case (Fig. 4).

3.3 Computing C_* from the mean wind divergence inside cold pools

It is assumed in the parameterization that cold pools are identical disks of radius r. This assumption makes it easy to determine C_* by the divergence theorem.

$$\int\int \mathrm{div}\left(\overrightarrow{V_{10\mathrm{m}}}\right) dS_{\rm wk} = C_* L_g \tag{23}$$

$$C_* = \frac{\overline{\text{div}\left(\overrightarrow{V_{10\text{m}}}\right)} S_{\text{wk}}}{L_g} \tag{24}$$

where S_{wk} is the surface of cold pools

$$S_{\text{wk}} = \pi r^2 \tag{25}$$

Equations 20, 21 and 25 allow us to express C_* as a function of the mean divergence of wind at 10 m, the surface fraction (σ_{wk}) and the density (D_{wk}) of cold pools by the relation:

$$C_* = \frac{1}{2}\overline{\text{div}\left(\overrightarrow{V_{10\text{m}}}\right)}\sqrt{\frac{\sigma_{\text{wk}}}{D_{\text{wk}}\pi}} \tag{26}$$

To apply this calculation of C_* in the LES, we take the horizontal average of the surface wind divergence inside cold pools. The surface fraction (σ_{wk}) of cold pools calculated in the LES is 0.214 (Average over the available time steps between 5:00 PM and 10:00 PM) for the AMMA case and 0.253 (Average over the 24 time steps with the SAM model) for the RCE case. To determine D_{wk}, we manually counted the centers of cold pools visible on the surface wind divergence maps (Fig. 2 and 3), as we did not use automated detection methods in this study that could generate their number automatically. We find a density, D_{wk}, of about 5 cold pools per 100 km $\times$ 100 km in the RCE case, and about 2.5 cold pools over the same domain in the AMMA case.

3.4 Computing ALP and ALE form gust front vertical velocities

Finally we derive a direct estimation of the Available Lifting Energy (ALE_{wk}) and Power (ALP_{wk}) in the LES from a sampling of the vertical wind at cloud base.

To do this, we first determine an average cloud-base height at which we extract vertical velocities $w_b(x, y)$. This height corresponds to the altitude at which the average profile of condensed water reaches its first non-zero value. It is estimated at around 950 hPa on the two oceanic LES and at around 750 hPa for the LES of the AMMA case (cf. Fig. 4).

We then separate the updrafts on gust fronts from those associated with thermal plumes. Since the updrafts on gust fronts are both stronger and more coherent horizontally than those associated with thermal plumes, we define a gust front mask based on a threshold applied to an horizontally moving average of the vertical velocity at cloud based w_b, denoted as $\tilde{w}_b(x, y)$. Because the gust fronts are stronger in the AMMA case than in the RCE case, different choices were made for the size of the horizontal box of the moving average (1.25 km$\times$1.25 km for the RCE case and 2 km$\times$2 km for AMMA) and for the value of the vertical velocity threshold (0.6 m/s for the RCE case and 2 m/s for the AMMA case). Those values were retained after several tests so as to separate as effectively as possible the gust front form other ascents.

Fig. 5 and 6 overlays the updrafts within (red) and outside (green) gust fronts on maps of T_{10m} anomaly (smoothed by applying a moving average with a box of 2.5 km$\times$2.5 km), for the RCE and AMMA cases respectively. The contours of the

	$D_{\mathbf{wk}}(10^{-10}$ m$^{-2})$	$\sigma_{\mathbf{wk}}$	σ_{gust}
RCE			
LES SAM	5	0.253	0.048
LES MESONH	5	0.264	0.017
AMMA			
LES MESONH	2.5	0.214	0.045

Table 1. Cold pools number density (D_{wk}), surface fraction of cold pools (σ_{wk}), and surface fraction of gust fronts (σ_{gust}) estimated from the LES for the RCE and AMMA cases. For the RCE case, the values represent an average over the 24 available time steps from the SAM LES and the 10 available time steps from the MESONH LES. For the AMMA case, the values are an average of the time steps obtained between 5:00 PM and 10:00 PM.

T_{10m} anomalies used to identify cold pools (-0.2 K for RCE and -1 K for AMMA) are displayed as well. Visually, the gust fronts computed with $\tilde{w}_b(x,y)$ thresholds of 0.6 m/s (RCE) and 2 m/s (AMMA) align well with the contours of cold pools identified using these T_{10m} anomaly thresholds. It also appears that most thermals are located in the environment of cold pools for both the RCE and AMMA cases. This retrospectively validates a choice made in LMDZ6A, where the effect of thermals was only computed outside cold pools.

Both ALE_{wk} and ALP_{wk} are computed from w_b restricted to the gust front mask, noted $w_{\text{b,gust}}$.

ALE_{wk} is estimated as the kinetic energy associated with the maximum value of $w_{\text{b,gust}}(x,y)$:

$$ALE_{\text{wk}} = \max(\frac{1}{2}{w_{\text{b,gust}}}^2) \tag{27}$$

ALP_{wk} represents the average updrafts power provided by all cold pools in the domain. It is calculated as the horizontal average of the cube of $w_{\text{b,gust}}$ times the surface fraction (σ_{gust}) covered by gust fronts:

$$ALP_{\text{wk}} = \sigma_{gust}\frac{1}{2}\rho\overline{w_{\text{b,gust}}}^3 \tag{28}$$

The gust front mask is used to calculate σ_{gust}, which is 0.048 (LES SAM) for the RCE case and 0.045 for the AMMA case, for the times shown in Fig. 5 and 6. Characteristics of the cold pools estimated from the sampling are gathered on Table 1.

3.5 Validation of phenomenological laws

Physical parameterizations are defined by sets of mathematical equations designed to represent subgrid processes within a column of the model. The formulation of these equations is based both on a phenomenological understanding of the processes involved and on fundamental principles of physics. These parameterizations can be evaluated as a whole or in parts, by isolating certain equations or relationships between internal variables, or between internal variables and GCM state variables. LES offers the possibility of performing a priori validation and adjustment of these laws.

In the cold pool model, variables ALE_{wk}, ALP_{wk} and C_* are determined from the collapse energy, $WAPE$ (see equations (4), (18) and (22)). We compare in Table 2 the values obtained using the parameterization formulations (parameterized value

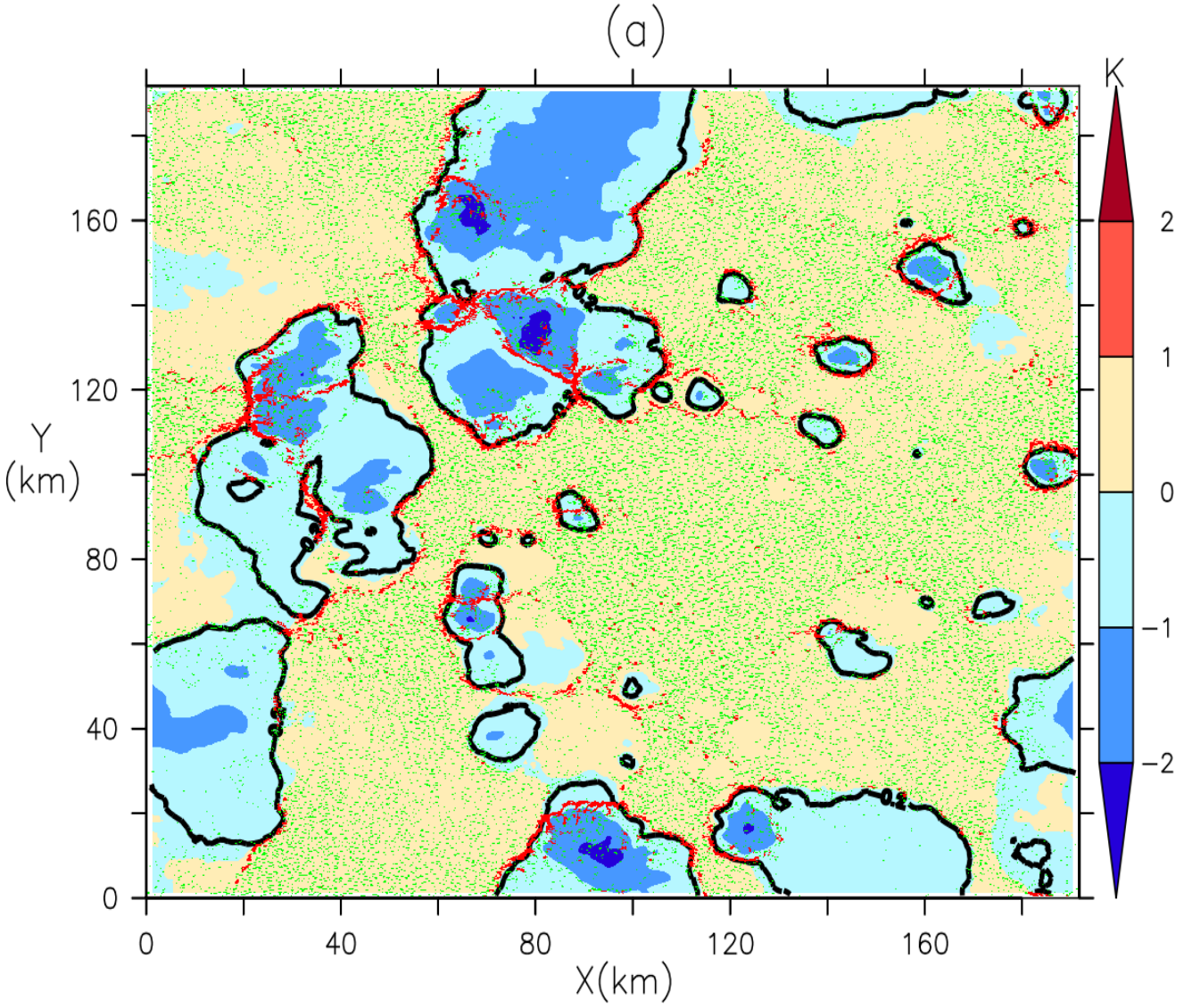

Figure 5. Map of $T_{10\mathrm{m}}$ anomaly (color shadings), smoothed (moving average with a horizontal box of 2.5 km×2.5 km), at an instant of the LES SAM of the RCE case. The black contour is the -0.2 K anomaly used to separate the inside from the environment of cold pools. The green and red dots show grid cells with vertical velocity at cloud base w_b larger than 0.8 m/s, inside (red) and outside (green) the gust front mask (see main text for the definition of the gust front mask).

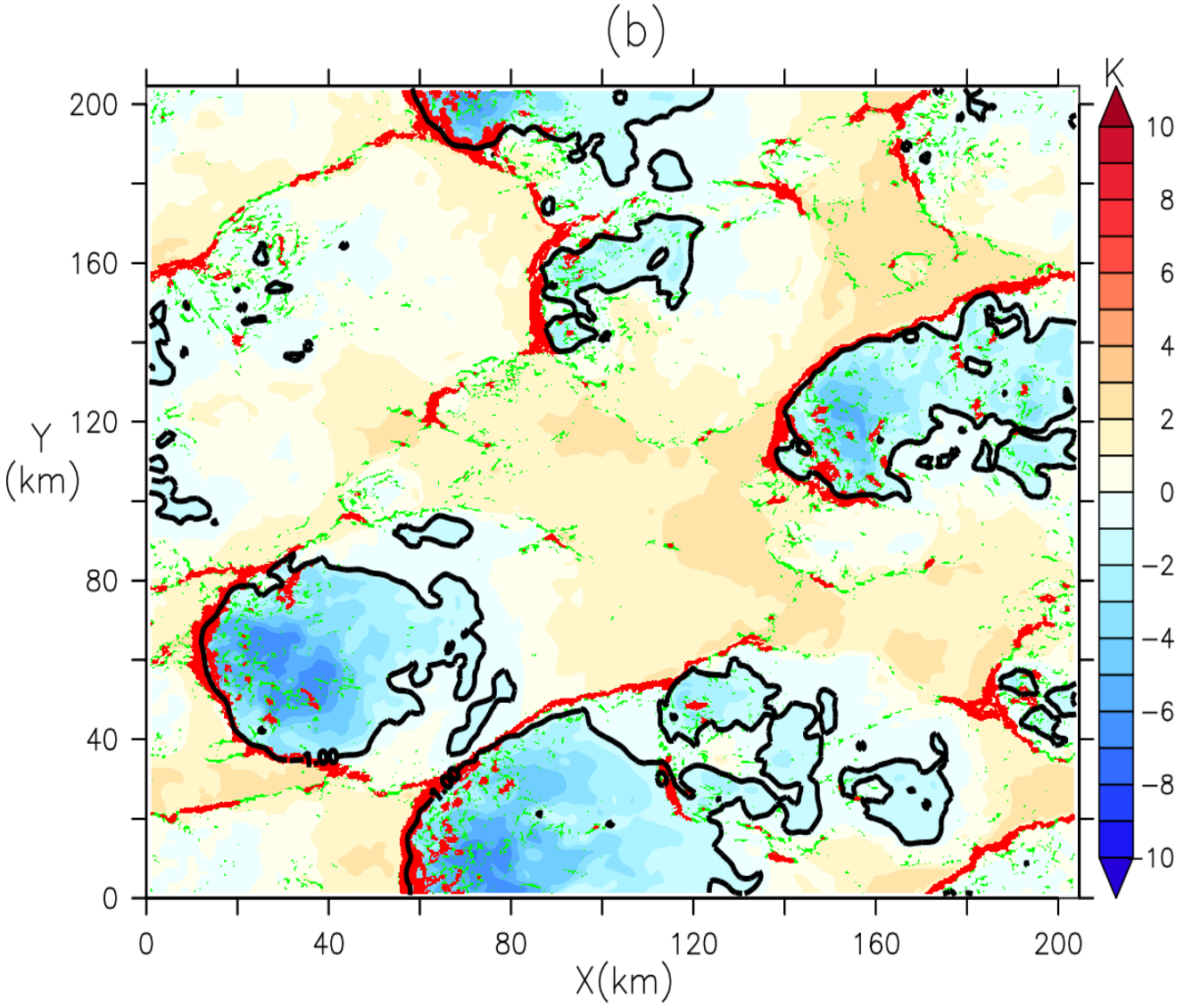

Figure 6. Map of $T_{10\mathrm{m}}$ anomaly (color shadings), smoothed (moving average with a horizontal box of 2.5 km×2.5 km), at 7:30 PM for the LES of the AMMA case. The black contour is the -1 K anomaly used to separate the inside from the environment of cold pools. The green and red dots show grid cells with vertical velocity at cloud base w_b larger than 2 m/s, inside (red) and outside (green) the gust front mask (see main text for the definition of the gust front mask).

from:	$ALE_{\mathbf{wk}}$ (J/kg) w_b sampl.	$WAPE$ (J/Kg) $\int \delta\theta_v$	C_* (m/s) div $\left(\overrightarrow{V_{10\mathrm{m}}}\right)$	C_* (m/s) P: k=0.33	C_* (m/s) P: k=0.56	$ALP_{\mathbf{wk}}$ (W/m^2) w_b sampl.	$ALP_{\mathbf{wk}}$ (J/kg) P: k=0.33	$ALP_{\mathbf{wk}}$ (W/m^2) P: k=0.56
RCE SAM	**10.460**	7.962	**2.228**	1.315	2.232	**0.054**	0.008	0.044
RCE MESO	**6.965**	7.912	**2.264**	1.313	2.228	**0.020**	0.008	0.044
AMMA MESO	**59.760**	45.870	**5.362**	3.133	5.316	**1.733**	0.279	1.368

Table 2. Comparison of the variables $WAPE$, ALE_{wk}, C_*, and ALP_{wk} obtained directly from the resolved wind in the LES (from w_b sampling or div $\left(\overrightarrow{V_{10\mathrm{m}}}\right)$), with those calculated using the formulations of the parameterization (parameterized values P, comming from the $WAPE$ computation based on the $\delta\theta_v$ profile). The S values are derived from the vertical velocity at cloud base (w_b) for ALE_{wk} and ALP_{wk}, from the mean divergence of wind at 10 m in cold pools for C_*, sampled directly from the LES. The P values are calculated from the $WAPE$ deduced from $\delta\theta_v$, itself sampled from the same LES, considering the coefficients k = 0.33 and k = 0.56. The analyses are based on the average of the available time steps: 24 time steps for the LES performed with SAM and 7 with MESONH in the oceanic RCE case, and between 5:00 PM and 10:00 PM for the LES of the AMMA case.

P), based on $WAPE$ deduced from $\delta\theta_v$, with those obtained directly from resolved wind in the LES (sampled value S): the vertical speed at cloud base (w_b) for ALE_{wk} and ALP_{wk}, and the mean divergence of wind at 10 m in cold pools for C_*. These analyses are performed by averaging over the available time steps: 24 time steps for SAM and 7 for MESONH in the RCE case, and between 5:00 PM and 10:00 PM for the AMMA case.

The values of ALE_{wk} calculated by both methods are very close to each other. The largest error is an underestimation by about 30% of the ALE_{wk} computed from $WAPE$ compared to the $w_{\mathrm{b,gust}}$ estimate. These results for the three LES confirm the validity of the hypothesis of equality between ALE_{wk} and $WAPE$ assumed in the parameterization.

Table 2 shows that, C_* values computed from the $WAPE$ are systematically lower than those coming from the mean divergence of wind at 10 m in cold pools. This difference could be due to an underestimation of the coefficient k, imposed here at 0.33. With $k = 0.56$, the calculation of C_* based on the $WAPE$ becomes comparable to those obtained from the mean divergence of wind at 10 m in cold pools (Table 2). As discussed above, the value of 0.33 was retained following an oral communication by Lafore (2000). But other studies propose different values: Lafore and Moncrieff (1989) estimate k at 0.68 based on CRM simulations of 2D squall grain, Bryan (2005) estimate it at 0.5 from observations of cold pools during the BAMEX experiment in the American Great Plains. Our results are thus compatible with the hypothesis of the model which postulates that the kinetic energy of cold pools results from the transformation of $WAPE$ into kinetic energy with a coefficient k compatible with the published estimates.

Table 2 also shows that, for the three LES cases, the values of ALP_{wk} calculated with $C*$ from $WAPE$ are at least three times lower than those obtained from $w_{\mathrm{b,gust}}$. Two coefficients are involved in the calculation of ALP_{wk} with the parameteri-

zation formula: the coefficient k and the lifting efficiency ϵ, imposed respectively to 0.33 and 0.25. Using k=0.56 however in the calculation of C_*, and keeping ϵ at is nominal value of 0.25 allows to reconcile the various estimates. This is compatible with the hypothesis of the parameterization according to which 25% of the horizontal power provided by the cold pools during its propagation would be used to reinforce the intensity of the convection while a large part dissipates.

4 Evaluation in the single column configuration of LMDZ

In this section, we evaluate the cold pool parameterization in the SCM configuration of LMDZ. The comparison is more demanding here, since all parameterizations interact with each other and because the state of the atmosphere at the time of evaluation depends on the interaction of all those parameterizations during the preceeding hours (AMMA) or days (RCE). The SCM simulations are performed with exactly the same initial and boundary conditions as the corresponding LES for both cases.

For the RCE case, we represent diagnostics once a quasi-steady state has been reached by averaging results between day 40 and 44.

In the AMMA case, cold pools appear around 5:00 PM in the LES but as early as 1:30 PM in LMDZ CTRL, revealing a model limitation. Adjusting the S_{trig} parameter involved in the triggering criteria could delay this onset, though a more physical approach would be required. For comparison, we focus on the times when cold pools are most developed: 7:30 PM in the LES and 2:30 PM in LMDZ CTRL, where the intermediate analysis of δT shows colder and thus more pronounced pools.

In order to facilitate comparisons between LMDZ and LES, we also impose in the LMDZ simulations the density of cold pools estimated in the LES. We thus set a density of 5 cold pools per 100 km$\times$100 km for the RCE case and 2.5 cold pools per 100 km$\times$100 km for the AMMA case. To represent the profiles of δT, δq and δw in LMDZ CTRL for the RCE case, we perform a time average between the 41st and 43rd day of simulation, in order to compare with the LES at the same times. For the AMMA case, the analysis is performed at 7:30 PM in the LES and at 2:30 PM in LMDZ CTRL, as specified above. The same procedure is applied to compare the $WAPE$, ALE, and ALP variables between LMDZ CTRL and the LES for both cases.

4.1 Vertical profiles of δT, δq and δw

The analysis of the δT profiles in the LES confirms that cold pools are colder at the surface with temperatures increasing towards the top for the three LES. The cold pools are about three times deeper in AMMA (Fig. 7a) than for the RCE case (Fig. 7d). In the LES, the cold pool temperatures for the AMMA case (around 4 K) are lower than those of the RCE case (around 1.2 K). This is consistent with observations which indicate much colder pools over land than over the ocean. For the AMMA case in particular, observations reveal a temperature drop of approximately 5 K during the passage of the cold pool (Lothon et al., 2011), a value fairly close to that of the LES. It should be noted however that the AMMA case corresponds to a relatively weak episode of continental convection. The δq profiles indicate that at the surface, cold pools are wetter than the surrounding air in the RCE case and the AMMA case (Fig. 7b and 7e). In both cases, the excess of humidity within cold pools

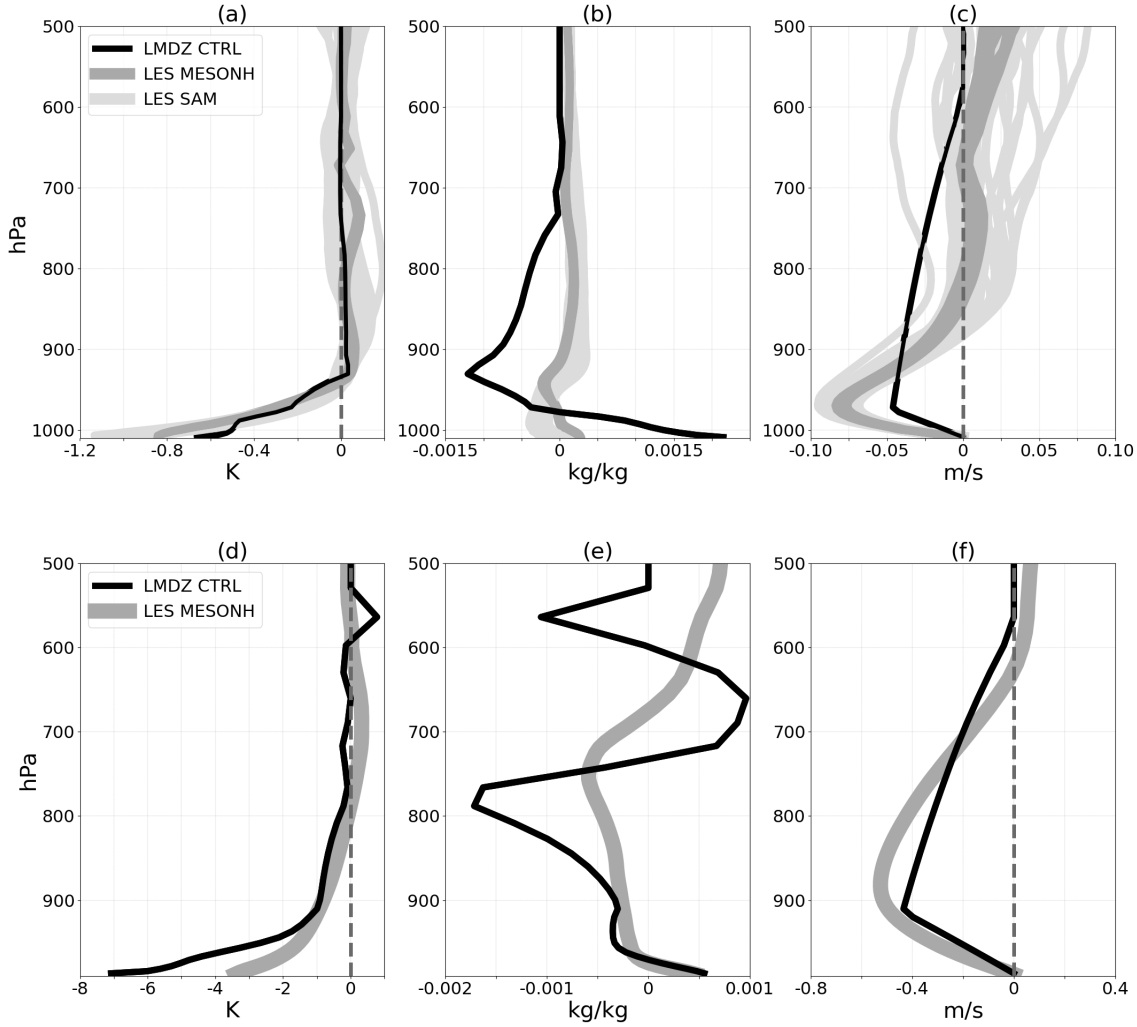

Figure 7. Vertical profiles of δT, δq and δw calculated in the LES and simulated by LMDZ control (LMDZ CTRL). For the RCE case (a, b, c), the profiles are shown for a set of 24 times for the SAM LES (light grey) and 10 for MESONH (dark grey). For LMDZ CTRL, results are averaged from day 41 to 43. For the AMMA case (d, e, f), the profiles correspond to the times when cold pools were most developed, i.e., 7:30 PM in LES and 2:30 PM in LMDZ CTRL.

	$WAPE$ (J/Kg)	$ALE_{\mathbf{wk}}$ (J/kg)	C_* (m/s)	$ALP_{\mathbf{wk}}$ (W/m^2)
RCE				
LES SAM	7.962	10.460	2.228	0.054
LES MESONH	7.912	6.965	2.264	0.020
LMDZ CTRL	2.957	2.957	0.802	0.001
AMMA				
LES MESONH	62.110	66.960	4.762	2.304
LMDZ CTRL	71.300	75.170	3.941	0.103

Table 3. Comparison of the $WAPE$, ALE_{wk}, C_* and ALP_{wk} computed from sampling of the LES and by LMDZ control (LMDZ CTRL) for the RCE case and the AMMA case. For the RCE case, comparisons are made using an average of the days following the achievement of equilibrium (days 41, 42, and 43). For the AMMA case, they are performed at the times when the cold pools are most developed (7:30 PM in the LES and 2:30 PM in LMDZ CTRL).

decreases with altitude up to the cold pools top. The humidity deficit above this level is due to the lateral entrainment of dry air from the mid troposphere and its subsidence into the cold pools (Fig. 7c and 7f). For the RCE case, this subsidence vanishes below 800 hPa (Fig. 7c), while for the AMMA case, it vanishes at a higher level, around 600 hPa (Fig. 7f).

The δT profiles simulated with LMDZ CTRL are qualitatively consistent with LES, with a cold pool top (where δT cancels) at about the right altitude. Cold pools simulated with LMDZ are however warmer than in the LES for the RCE case (Fig. 7a), and colder at the surface than the LES for the AMMA case (Fig. 7d). Consistently with LES, cold pools are also wetter at the surface and drier close to their top top (Fig. 7b and Fig. 7e). However the variations of δq are much larger in LMDZ than in the corresponding LES. In particular, the cold pools are much too dry at their top in LMDZ. In both cases, cold pools are associated with subsidence. The height at which the subsidence of air masses into cold pools begins, fixed at 600 hPa in LMDZ CTRL, is too high compared to LES for the RCE case (Fig. 7e).

4.2 WAPE, ALE and ALP

For the RCE case, the $WAPE$ is significanlty smaller in LMDZ CTRL than in the LES, with a difference of at least a factor of 2 (Table 3). These low values of $WAPE$ in LMDZ CTRL also translate into low ALE_{wk} values compared to LES (Table 3). On the other hand, for the AMMA case, the $WAPE$ simulated by the model, and consequently ALE_{wk}, are slightly higher than the values derived from the LES (Table 3). The value of C_* simulated by LMDZ CTRL is at least three times smaller than that of the LES in the RCE case and slightly lower for the AMMA case (Table 3). ALP_{wk} is at least twenty times weaker in LMDZ CTRL than in the LES for all cases (Table 3).

Various modifications of the cold pool parameterization are explored in the following section to try to correct the defects listed above.

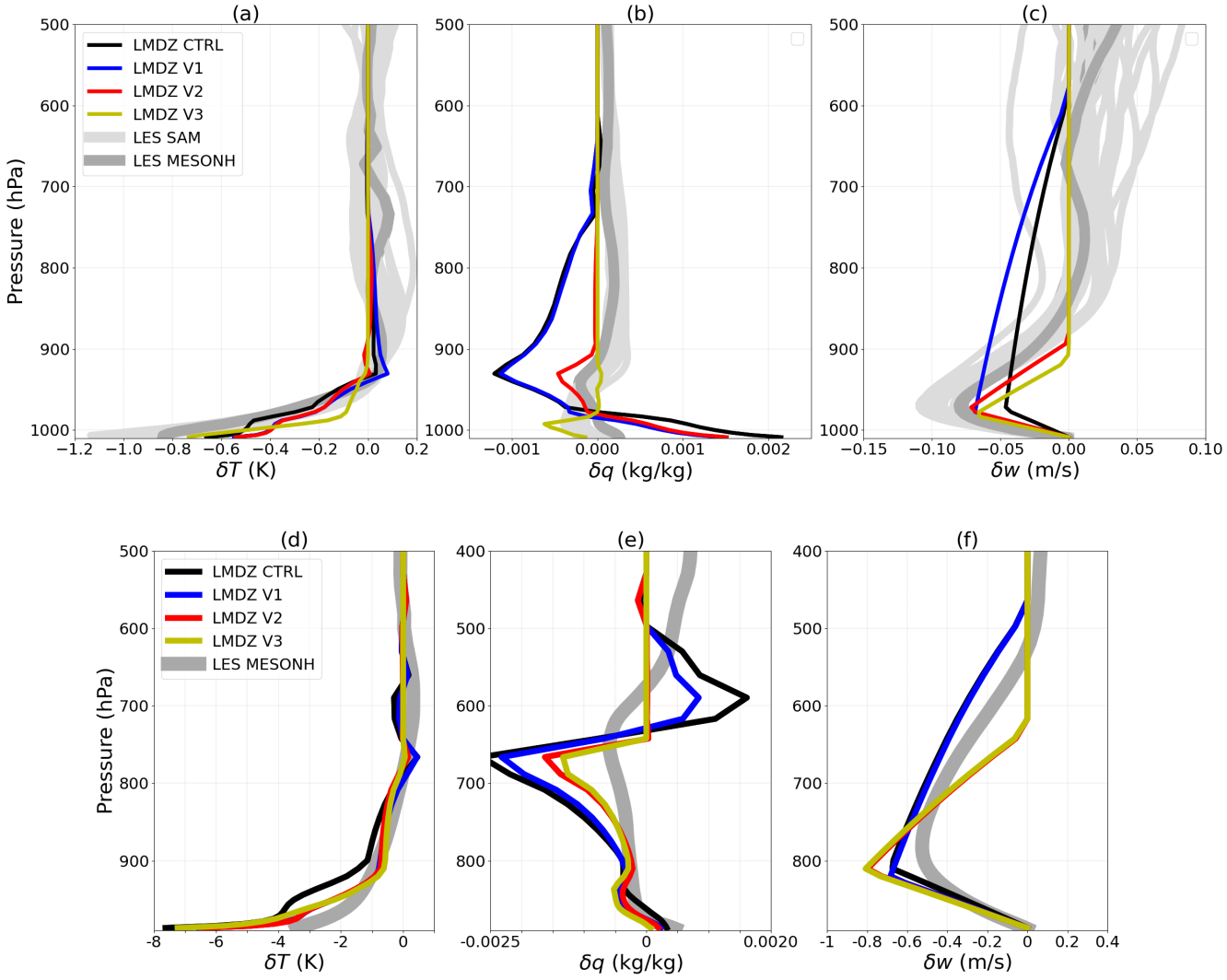

Figure 8. Vertical profiles of δT, δq and δw calculated in the LES and simulated with LMDZ: for a control simulation (CTRL, same curves as Fig. 7), with adjustment of the coefficient k to 0.56 (V1), with the modified computation of p_{upper} (V2) and with the activation of thermals in the entire domain (V3). Both the RCE (a, b, c) and AMMA (d, e, f) cases are shown for the times as in Fig. 9.

5 Improvements of the cold pool model

Here, we start by correcting the identified discrepancies between the LES and the model concerning the value of the coefficient k and the pressure height p_{upper}, and by assessing the impact of these changes on the temperature and humidity difference between the cold pools and their environment, before exploring other avenues for improvement.

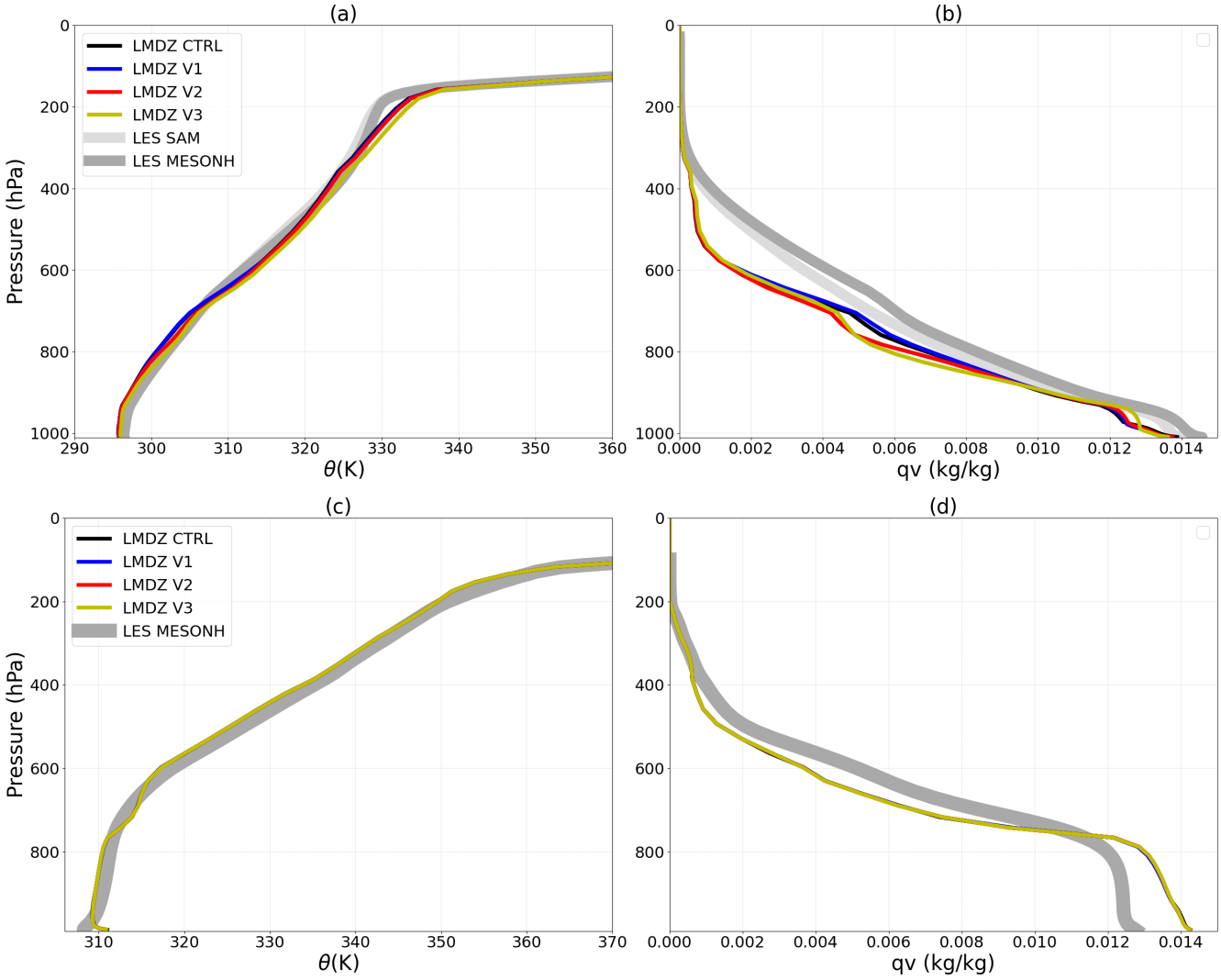

Figure 9. Vertical profiles of potential temperature (θ) and specific humidity (qv) calculated in the LES and simulated with LMDZ: for a control simulation (CTRL), with adjustment of the coefficient k to 0.56 (V1), with the modified computation of p_{upper} (V2) and with the activation of thermals in the entire domain (V3). Both the RCE (a, b) and AMMA (c, d) cases are shown for the same times as in Fig. 7

Simulations	Protocols
LMDZ CTRL	simulation of LMDZ with the standard configuration except that D_{wk} is set to 5 per 100×100 km^2 for the RCE case and 2.5 for AMMA
LMDZ V1	LMDZ CTRL + change of k to 0.56
LMDZ V2	LMDZ V1 + changed computation of p_{upper}
LMDZ V3	LMDZ V2 + activation of thermals throughout the domain

Table 4. Description of simulations performed with LMDZ in the standard configuration and with various modifications

5.1 Coefficient *k*

We present here the impact of increasing the coefficient k from 0.33 to 0.56 (LMDZ V1 simulation) on the profiles of δT, δq, δw as well as on the variables C_*, $WAPE$, ALP_{wk} and ALE_{wk} (see Table 4). In the RCE case, this modification significantly improves the profile of δw below p_{wk} (Fig. 8c). It also allows for a better representation of the δw profiles below p_{wk} in the AMMA case (Fig. 8f). These improvements are directly linked to the increase in C_* for both cases (Table 5), since the δw profile below p_{wk} depends on the spreading of cold pools. The increase in C_* could be associated with stronger air mass subsidence within the cold pool, which would contribute to a slight drying near the surface in both cases (Fig. 8b and 8e). For the AMMA case, this drying results in slightly drier cold pools at the surface in LMDZ V1 than in the LES, but they remain overall comparable to the latter. The increase in C_* in both the RCE and AMMA cases also leads to a better representation of ALP_{wk} (an increase by at least a factor of 5 for both cases), even though this variable remains underestimated (Table 5). We also note a warming effect from this modification in both the RCE and AMMA cases. The impact on the δT profiles in the AMMA and RCE cases is responsible for the decrease in the values of $WAPE$ and ALE_{wk} for these two cases (Table 5).

Fig. 9 shows that the modification introduced in version V1 has a low impact on the θ and qv mean profiles (Fig. 9), the black and blue curves being almost superimposed. Both CTRL and V1 simulations reproduce the θ profiles fairly well. Around 600 hPa, the temperature is too warm in the RCE case. Regarding humidity, a dry bias is present in the boundary layer in the RCE case, as well as between 800 and 400 hPa. For the AMMA case, there is a wet bias in the boundary layer and above 600 hPa, and a dry bias between 700 and 600 hPa.

5.2 Choice of cold pools scheme upper bound, p_{upper}

In the previous sections, we found that the altitude at which the subsidence of dry air above cold pools initiate is located around 800 hPa in the LES for the RCE case and around 600 hPa for the AMMA case, while in LMDZ, p_{upper} is arbitrarily set to 600 hPa in the original version of the parameterization. In version V2, in addition to the change of the value of k from 0.33 to 0.56, we impose $p_{\text{srf}} - p_{\text{upper}} = \gamma_{\text{wk,upper}}(p_{\text{srf}} - p_{\text{wk}})$ with $\gamma_{\text{wk,upper}}$, fixed here to 3, is considered as a new free parameter in the following section.

Note that the numerical scheme used to estimate $p_{\rm wk}$ was also modified compared to GL10 in order to solve instability issues. The principle of the new scheme is to compute the height at which the vertical integral, from the surface up to the first positive value, of $\delta\theta$ reaches a fraction χ of the total integral. This fraction is taken slightly below 100% to avoid fluctuations of $p_{\rm wk}$ from one time step to the other, which happens when $\delta\theta$ is close to zero on a large range of altitudes around $p_{\rm wk}$ as seen in Fig. 7 and Fig. 8. The new computation was activated already in CTRL and V1, not affecting the results significantly (figure not shown). The new computation becomes really important when $p_{\rm upper}$ is deduced from $p_{\rm wk}$ rather than being imposed.

Comparisons between LMDZ V2 simulations and LES show a better representation of the δq profiles at the top of cold pools in both the RCE and AMMA cases (Fig. 8b and 8e). These results show that the dry bias at the top of the cold pool in the original version was due to advection of dry air from too high an altitude. This modification also reduces slightly the humidity of cold pools near surface in the RCE case, although they remain more humid than in the LES. Note finally that this modification has a very limited impact on the δT profiles.

Table 5 shows that the change in $p_{\rm upper}$ weakly affects the variables $WAPE$, C_*, $ALE_{\rm wk}$ and $ALP_{\rm wk}$ for these two cases.

Versions V2 does not modify much the mean vertical profiles except for a drying of the mid-troposphere in the RCE case (Fig. 9b), in a region where the CTRL simulation was already too dry. Although the time evolution of the mean profiles is the first target of physics parameterizations, we think however that the improvement of the internal variables is so strong for this modification that it should be adopted in the future in LMDZ.

5.3 Activation of thermals throughout the domain

As explained above, in the standard LMDZ configuration, thermals only interact with temperature and humidity profiles outside cold pools, inducing a differential heating in moistening (equation (8)). This choice was originally made to account for the fact that the atmosphere is more stable inside cold pools, and indeed the analysis above shows that the thermal plumes that reach cloud base are essentially located outside cold pools. Version V3 is identical to version V2, except that we consider that thermal plumes are active everywhere in the grid cell. Consistently, the terms ${Q_1}^{\rm th}$ and ${Q_2}^{\rm th}$ are removed from (8). For the RCE case, this leads to a decrease in the surface humidity of cold pools, closer to the LES results (Fig. 8b). In the AMMA case, the effect is also present, although less pronounced (Fig. 8e). This result is expected because the vertical transport by thermals systematically dries the surface (Diallo et al., 2017). This confirms the key role of boundary layer convection in regulating surface humidity on both continent (Diallo et al., 2017) and ocean (Hourdin et al., 2020), via the mixing of moist air with dry air above. One way to improve the representation of humidity anomaly profile without activating the thermal plumes everywhere would be to add a simple parameterization of shallow and cloud-free boundary layer convection (a simplified version of the thermal plume model) within the cold pool region.

In version V3, cold pools are colder than in version V2 in both the RCE and AMMA cases (Fig. 8). In the RCE case, however, cold pools remain less cold than in the LES despite this effect. In the AMMA case, this cooling accentuates the overestimation of the cold anomaly. In both cases, this cooling leads to an increase in the $WAPE$, C_*, $ALE_{\rm wk}$, and $ALP_{\rm wk}$ variables (Table 5). Version V3 does not introduce any notable changes, compared to V2, in the profiles of θ and q_v for the RCE and AMMA cases.

	$WAPE$ (J/Kg)	$ALE_{\mathbf{wk}}$ (J/kg)	C_* (m/s)	$ALP_{\mathbf{wk}}$ (W/m^2)
RCE				
LES SAM	7.962	10.460	2.228	0.054
LES MESONH	7.912	6.965	2.264	0.020
LMDZ CTRL	2.957	2.957	0.802	0.001
LMDZ V1	2.663	2.663	1.292	0.004
LMDZ V2	2.620	2.620	1.282	0.004
LMDZ V3	3.585	3.585	1.500	0.0055
12 bests	[5.1,5.3]	[5.1,5.3]	[1.79,1.83]	[0.013,0.025]
AMMA				
LES MESONH	62.110	66.960	4.762	2.304
LMDZ CTRL	71.300	75.170	3.941	0.103
LMDZ V1	56.930	56.930	5.975	0.234
LMDZ V2	57.990	57.990	6.031	0.252
LMDZ V3	58.190	58.190	6.041	0.334
12 bests	[40,60]	[40,60]	[4.5,5.1]	[0.5,2.5]

Table 5. Comparison of the variables $WAPE$, ALE_{wk}, C_* and ALP_{wk} calculated from the samplings in the LES, with those obtained with LMDZ: in a control simulation (CTRL), with the adjustment of the coefficient k to 0.56 (V1), with the modified computation of p_{upper} (V2), the activation of thermals in the entire domain (V3) and for the 12 best simulations of a tuning experiment, for the RCE and AMMA cases.

5.4 Tuning of free parameters

The tests presented above show possible avenues for improving the cold pool parameterization. However, we see that the modifications do not sufficiently affect the mean profiles to reduce these biases significantly. All tests underestimate (for the RCE case) or overestimate (for the AMMA case) the cold temperature anomaly inside cold pools, as well as $WAPE$, ALE_{wk}, C_*, and ALP_{wk}. We also observe systematic errors in the mean profiles, notably profiles that are much too dry for the RCE case.

In the GCM, these variables are not sensitive only to the parameters or formulation of the cold pool model. They are influenced by all other parameterizations, and in particular by the convection scheme to which the cold pool scheme is strongly coupled. In an attempt to see how modifications to other parameterizations could help reduce these biases, we performed automatic calibration simulations using the `htexplo` tool.

In practice, we decided to start from a tuning performed for the convective boundary layer by Hourdin et al. (2021), for a configuration with 95 levels rather than 79 and using more recent versions of the codes than those used in the rest of the paper. This version indeed serves as the basis for preparing the future version of the climate model for the FastTrac part of the CMIP7

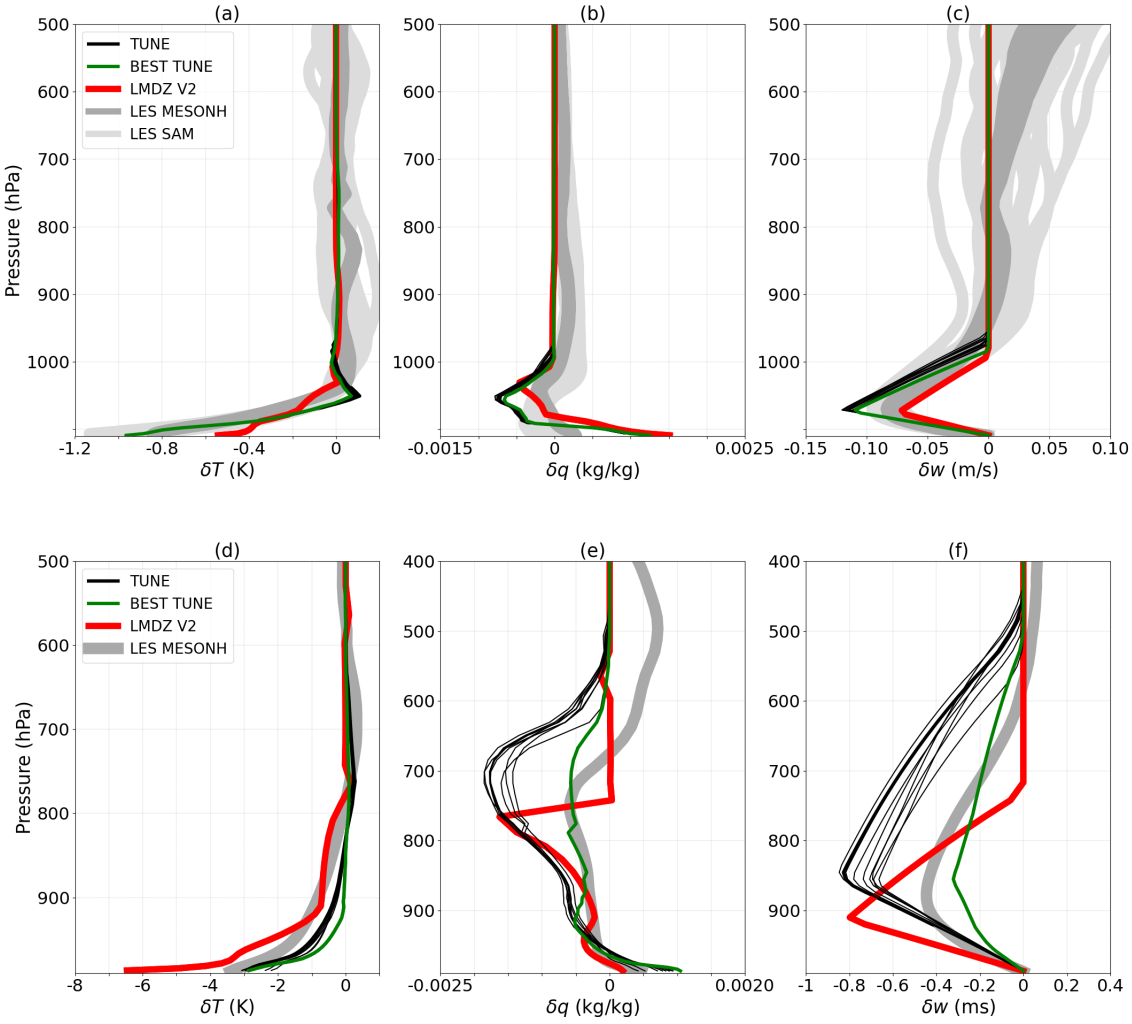

Figure 10. Like Fig. 8, but showing for LMDZ, the V2 simulation, the 12 best simulations from the tuning (TUNE, in black) as well as the best one among them (TUNE BEST, in green).

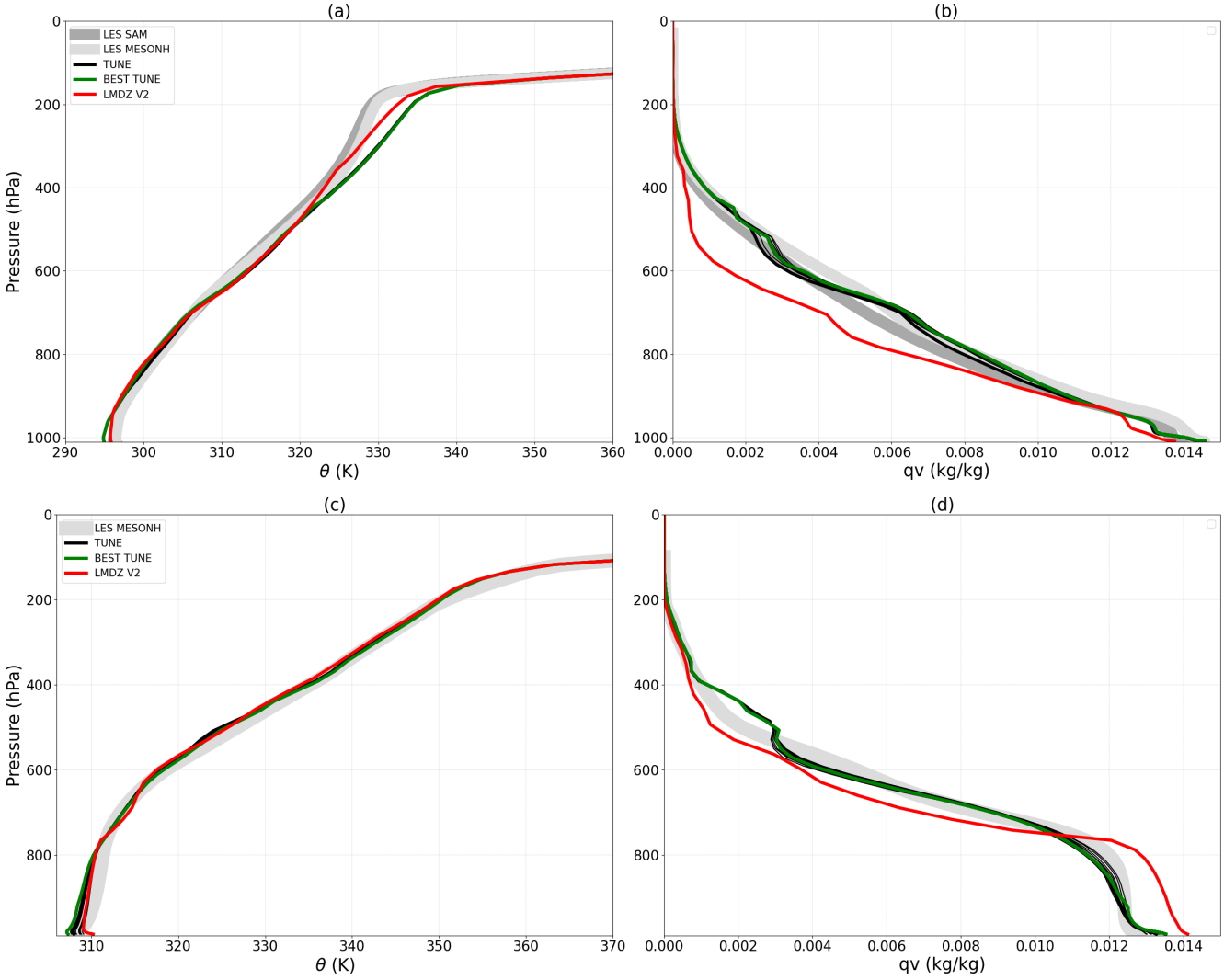

Figure 11. Like Fig. 9, but showing for LMDZ, the V2 simulation, the 12 best simulations from the tuning (TUNE, in black) as well as the best one among them (TUNE BEST, in green).

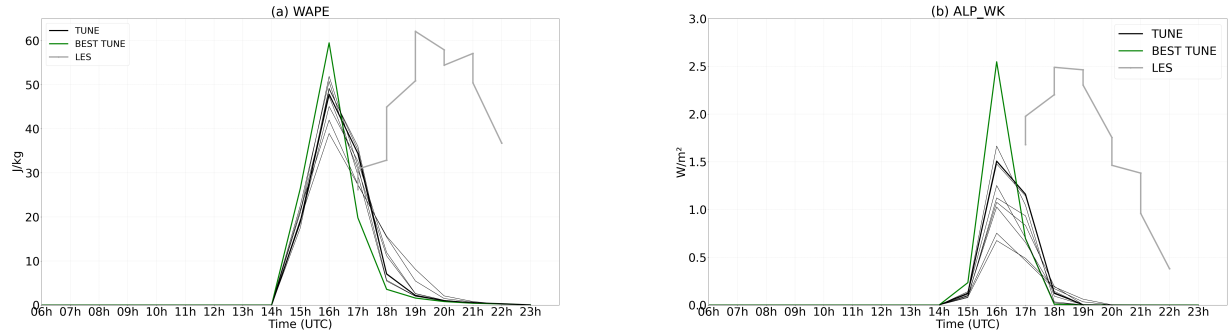

Figure 12. Time series of the collapse energy, $WAPE$ (J/kg, panel a), and the available lifting power,ALP_{wk} (W/m^2, panel b), associated with cold pools, shown for the 12 best simulations from the tuning (TUNE, in black), for the best among them (TUNE BEST, in green) and for the LES (in grey) over times steps between 5:00 PM and 10:00 PM

project, whose simulations are scheduled to begin in early 2026. We assume that the boundary layer parameters have already been optimized to accurately represent the convective boundary layer and associated clouds, cumulus and stratocumulus. Regarding modifications to the cold pool model, those affecting the coefficient k and p_{upper} are taken into account, as in the V2 configuration. Adjustments related to thermals (V3) are not considered here because they raise as many questions as they solve.

The tuning is performed using the `htexplo` tool as explained in Appendix A. We choose metrics preferentially on the RCE case targeting the WAPE, ALP and the profiles of anomalies and mean variables. Indeed, we wish to avoid being overly dependent on errors in the phasing of the deep convective diurnal cycle. The adjustable parameters selected for the cold pool model are: k, $\gamma_{\text{wk,upper}}$, χ, and ϵ. Parameters involved in the deep convection scheme are also included: the minimum wb_{srf} and maximum wb_{max} vertical velocities at the base of the convective column; the fraction of the grid cell area in which precipitating downdrafts occur, σ_{desc}; and the maximum precipitation efficiency in the Emmanuel scheme (EP_{max}). This efficiency is a maximum efficiency at the top of the convective columns. The difference 1-EP_{max} controls how much condensed water exits the convective clouds, and thus the moisture source in the upper atmosphere. Details on the metrics and parameter ranges chosen are given in Appendix A.

The result of this tuning is the product of extensive trial and error regarding the choice of parameters, their bounds, the metrics to adjust, and the associated tolerances. We present here the 12 best simulations resulting from 13 waves of tuning. Among them, the simulation considered to be the most performant (TUNE BEST) is also identified. The analysis of the results for the RCE case reveals that the simulations improve the representation of the targeted variables, particularly the mean humidity profile and the amplitude of the potential temperature deviations $\delta\theta$. These deviations are more negative, consistent with a stronger WAPE and C_* coefficient. Furthermore, the δq profiles at the top of the cold pools, as well as the δw profiles, remain well represented across all 12 simulations.

By applying the parameters from the tuning performed on the RCE case to the AMMA case simulations, a significant reduction in the cold bias at the surface of cold pools is obtained (Fig. 10d), as well as an improvement in the mean humidity profiles across all 12 simulations. Only the results from the BEST TUNE simulation reproduce δq and δw profiles consistent with the LES, the others tending to generate cold pools that are too dry at their top due to slightly overestimated δw profiles (Fig. 10e and 10f). The BEST TUNE simulation also provides a better representation of $WAPE$ (Fig. 12a) and ALP_{wk} (Fig. 12b) in the AMMA case, with values very close to those from the LES at the time when cold pools reach their maximum development (Table 5), despite a shift by about 3 hours earlier in the afternoon. Nevertheless, a moist bias and a cold bias persist in the boundary layer.

Several lessons can be learned about the range of the free parameters involved in the tuning when considering the best values (last column of Table B1). First the fraction of the grid cell assigned to unsaturated downdrafts, σ_{desc} with a selected range of $[0.042, 0.048]$, is larger than the nominal value of 0.015, which contributes to first order to the increased intensity of cold pools, in particular for the RCE case. Concerning the parameters of the cold pool model itself, first the tuning of k from (4) confirms the findings of Section 3.5, with selected range of $[0.56, 0.57]$. The value of $\gamma_{\text{wk,upper}}$ that controls the height of the cold pool model is $[3.6, 4.1]$, compatible as well with the previous findings. With a range of $[0.26, 0.46]$, the tuning suggest that more than 25% of the power associated with cold pool spreading is available for deep convection. Note finally that the χ parameter of the new numerical scheme for p_{wk} computation is also strongly constraint by the tuning exercise (to a value of about 0.97). This exercise confirms the extraordinary progress represented by the availability of automatic retuning methodology.

6 Conclusions

Although the cold pool model proposed by Grandpeix and Lafore (2010) has improved the representation of convection in the LMDZ climate model (Rio et al., 2009), its internal variables and physical properties had never been evaluated in details so far. This work proposes, for the first time, a detailed evaluation of the cold pool model, based on LES. We evaluate both the physics of the model, its internal variables and those involved in the coupling with deep convection, based on two oceanic LES in the RCE regime and a continental LES of the AMMA case.

For this, we introduce two samplings of the LES. The first one separates the interior from the outside of the cold pools, based on a threshold of the 10 m temperature anomaly of -0.2 K for the RCE case and -1 K for AMMA. The second one separates the zone of gust fronts by smoothing horizontally the vertical wind at cloud base (moving average over a square of 1.25 km side for the RCE case and 2 km for AMMA) with a threshold of 0.8 m/s for the RCE case and 2 m/s for AMMA. The coincidence of the temperature contour used for the cold pool sampling with the lines of maximum wind converge near the surface and with the gust front mask provides a very consistent view of the cold pools. It reinforces the choices that guided the conception of the cold pool scheme. It also confirms that most of the thermals reaching cloud base are located outside cold pools.

We started by validating relationship internal to the parameterizations, by diagnostics of the LES. The results show that the ALE_{wk} calculated from the $WAPE$ (computed from the vertical profile of the temperature anomaly between the cold pool and its environment) is comparable to that estimated from the vertical velocity in gust fronts $w_{\text{b,gust}}$. This result is consistent

with the model hypothesis, which estimates an equality between $ALE_{\rm wk}$ and $WAPE$. The spreading speed C_*, determined from the mean of divergence of wind at 10 m inside cold pools, is consistent with the estimate based on the square root of $WAPE$, if coefficient k entering in equation ((4)) is fixed to 0.56, a value consistent with published values Bryan (2005); Lafore and Moncrieff (1989). $ALP_{\rm wk}$, calculated using C_* (computed from the $WAPE$ with $k = 0.56$), is close to the estimate derived directly from $w_{\rm b,gust}$. This result is compatible with the model hypothesis according to which a quarter of the cold pool Avaliable Potential Power, $ALP_{\rm wk}$, feed deep convection, the remaining being dissipated. All of these results show the overall consistency of the model hypotheses with the three LES (RCE and AMMA) used in this study.

We then compare LES results with the SCM version of LMDZ. The results show that the initial version of the parameterization represents the cold pool properties well to first order, but with a dry anomaly in the cold pool region much too strong for the RCE case above the cold pool top, and a general tendency for both cases to underestimate the cold anomaly within cold pools and in turns $WAPE$, C_*, $ALE_{\rm wk}$ and $ALE_{\rm wk}$.

The dry bias simulated at the top of cold pools is attributed to the pressure of the maximum subsidence height ($p_{\rm upper}$) which was imposed at a fixed value of 600 hPa in the original scheme. This value which was inspired from continental situations is well suited for the AMMA case but much to small for the RCE case for which the LES indicate a value of about 800 hPa. By making $p_{\rm upper}$ dependent on $p_{\rm wk}$, the pressure at cold pool top, we significantly improve the simulated humidity at the top of cold pools for both cases. These results highlight the control of the cold pool humidity anomaly profile by lateral entrainment of dry air from the mid troposphere and subsidence within the cold pool. They also confirm the relevance of the cold pool transport model with lateral entrainment between $p_{\rm upper}$ and $p_{\rm wk}$ feeding the maximum subsidence at $p_{\rm wk}$.

Increasing the value of coefficient k from 0.33 to 0.56, as suggested by the analysis of the LES, almost doubles the estimation of C_* for both the RCE and AMMA cases and multiplies the value of $ALP_{\rm wk}$ by 6 for AMMA and more than 10 for the RCE case, without affecting much the vertical mean and anomaly profiles. However, despite this improvements, C_* and $ALP_{\rm wk}$ remain underestimated in both cases.

A wet bias is also obtained at the surface of cold pools in the RCE and AMMA cases. Our analyses show that this bias is linked to the absence, in the model, of the effect of thermals on the variation of humidity at the surface of cold pools. The evaporation flux plays a weak role in this variation, which seems to be mainly controlled by thermals.

Despite all the improvements, the cold pools remain not cool enough in the RCE case, inducing an underestimation of C_* by about 25% and $ALP_{\rm wk}$ by a factor of 3. In the AMMA case, where the cold pools are colder, the value of C_* is, conversely, overestimated by about 35%, while that of $ALP_{\rm wk}$ remains underestimated by a factor of 4. In order to check whether this limitation may come from a coupling with the other model parameterizations, and in particular that of deep convection, we conducted a calibration experiment using the HighTune explorer software to jointly adjust the free parameters of the cold pools and deep convection models. This tuning procedure also aimed to correct the dry and wet biases still present in the potential temperature and specific humidity profiles.

These adjustments led to a significant improvement in the representation of cold pool temperature, as well as specific humidity for the RCE and AMMA cases, even if a humid and cold bias persists in the boundary layer for the AMMA case. The values of $WAPE$, $ALP_{\rm wk}$ and C_* are also improved.

The above mentioned changes have been adopted in the new version of the LMDZ global model, used as the atmospheric component of the IPSL-CM7 coupled model under development for the forthcoming CMIP7 Fast-Trac exercise.

Although significant progress has been made in recent years in modeling cold pools, due to their important role in convection, challenges remain. First a simple parameterization of boundary layer convective transport, based for instance on a simplified version of the thermal plume model, could be included to better represent vertical mixing within the cold pools without activating the thermal plume model uniformly over the grid cell. The cold pool number density should become an internal variable of the model since we know it presents very different values when considering popcorn like convection over ocean or continents, or well organized long live system such as squall lines. A parameterization of this number density, based on a population dynamic model is presently under test. To end with, the issue of the propagation of cold pools from grid cell to grid cell needs to be also integrated into GCMs.

TEXT

Code and data availability. The software used are distributed openly through `subversion` at address: LMDZ :
`htexplo`:
The data and scripts used to make the figures of the document will be made available as well on a DOI if the article is accepted for publication.

Appendix A: and the tuning setup

A1 High-Tune Explorer (`htexplo`) tool

The tuning experiments shown here are done with the `htexplo` tool.

`htexplo` has been developed in collaboration between the LMD (Paris), the Centre National de Recherche Météorologiques (CNRM/Météo-France) and the University of Exeter (UK). It is an automatic calibration tool for free parameters, based on machine learning techniques from the uncertainty quantification community (Williamson et al., 2013). This approach proposes a new calibration paradigm: instead of optimizing parameter values, it aims to identify the subset of parameters that enables the model to reproduce certain observables to a certain accuracy. The main steps involved in using the tool, as well as its mathematical foundations, are well described in Couvreux et al. (2021). The `htexplo` tool was used for the first time in a SCM/LES comparison on several boundary layer cases of the LMDZ model, in order to characterize the subspace of free parameter values for which SCM simulations are consistent with LES for certain metrics and a given tolerance (Couvreux et al., 2021). This information was then used by Hourdin et al. (2021) to calibrate the 3D configuration. These authors demonstrated how reducing the parameter space using this method significantly saves computing and human resources. They also pointed out that this approach eases the burden on the modeler, enabling him or her to concentrate more on understanding and improving the physical parameterizations of the model.

metric	unit	target	tolerance
RCE case, average from day 41 to day 43			
WAPE	$m^2\ s^{-2}$	8	2
C_*	$m\ s^{-1}$	2.2	0.2
$\delta\theta_{0\text{-}50\ m}$	K	-0.83	0.045
$\delta\theta_{0\text{-}600\ m}$	K	-0.48	0.063
$qv_{0\text{-}500\ m}$	g/kg	14.1	0.45
$qv_{1\text{-}3\ km}$	g/kg	9.14	0.45
$qv_{5\text{-}6\ km}$	g/kg	2.55	0.33
$qv_{8\text{-}10\ km}$	g/kg	0.289	0.063
$\theta_{0\text{-}500\ m}$	K	296.5	1.47
$\theta_{1\text{-}3\ km}$	K	301.0	1.
$\theta_{5\text{-}6\ km}$	K	317.4	1.
$\theta_{8\text{-}10\ km}$	K	328.8	3.
AMMA case, average from 10:00 AM to 5:00 PM			
WAPE	$m^2\ s^{-2}$	20	3

Table A1. Metrics (targets and 1-σ tolerances) used for the tuning. For the RCE case, they concern the averages between days 41 and 43 of the WAPE and the cold pool spreading rate C_*, as well as the vertical profiles of $\delta\theta$, qv, and θ averaged over the altitude ranges specified in the right column. For the AMMA case, only the WAPE averaged between hours 10 and 17 of the simulation is used.

For the RCE case, we target the quasi-equilibrium phase by considering averages between days 41 and 43. The metrics selected for these calibration exercises are the profiles of δT, q_v, and θ, evaluated from vertical averages at different levels as indicated in.

Details on the metrics, with targets and tolerances to error, are given in Table A1.

660 The parameters chosen for tuning are listed in Table B1 together with the a priori ranges given to `htexplo` at the beginning of the tuning exercise and ranges of the best 12 simulations obtained after 13 waves of tuning.

Author contributions. Mamadou Lamine Thiam: conception of the work, diagnostics, analysis, figures and writing
Frédéric Hourdin: conception of the work, diagnostics, analysis and writing
Jean-Yves Grandpeix: conception of the work, analysis and writing

Parameter	units	[min,max] prior	exploration	[min , max] 12 best simulations
Cold pool model				
ϵ ((19))	-	[0.25 , 0.5]	linear	[0.26 , 0.46]
$\gamma_{\text{wk,upper}}$	-	[3.5 , 5]	linear	[3.6 , 4.1]
k ((4))	-	[0.33 , 0.66]	linear	[0.56 , 0.57]
χ	-	[0.75 , 0.99]	linear	[0.96 , 0.987]
Convection model				
wb_{srf}	m/s	[0.5 , 1.2]	linear	[0.55 , 0.98]
wb_{max}	m/s	[2.8 , 6]	linear	[2.8 , 3.5]
σ_{desc}	-	[0.015 , 0.05]	linear	[0.042 , 0.048]
1-EP_{max}	-	[0.05 , 0.1]	log	[.93 , .95]
$k_{\text{ALP,BL}}$	-	[0.2 , 0.5]	linear	[0.33 , 0.47]

Table B1. Free parameters considered in the tuning exercise.

Catherine Rio: analysis and writing

Maëlle Coulon-Decorzens: tuning expertise

Competing interests. None

Disclaimer. None

Acknowledgements. The authors thank Caroline Müller for providing the RCE simulation run with the SAM model and Fleur Couvreux for providing the AMMA simulation run with the MESO-NH model. We also acknowledge support from the DEPHY research group of CLIMERI, funded by CNRS/INSU and Météo-France. The work is part of and was supported by the DEPHY french national project. It benefited from the development of the `htexplo` tool within this project and automation of LES/SCM simulations through standardization of IO formats. Mamadou Lamine Thiam PhD was supported by [Nom du programme]

References

Böing, S. J., Jonker, H. J., Siebesma, A. P., and Grabowski, W. W.: Influence of the subcloud layer on the development of a deep convective ensemble, Journal of the Atmospheric Sciences, 69, 2682–2698, 2012.

Boucher, O., Denvil, S., Levavasseur, G., Cozic, A., Caubel, A., Foujols, M.-A., Meurdesoif, Y., Balkanski, Y., Checa-Garcia, R., Hauglustaine, D., et al.: IPSL IPSL-CM6A-LR-INCA model output prepared for CMIP6 RFMIP piClim-aer, 2020.

Brown, A., Cederwall, R. T., Chlond, A., Duynkerke, P. G., Golaz, J.-C., Khairoutdinov, M., Lewellen, D., Lock, A., MacVean, M., Moeng, C.-H., et al.: Large-eddy simulation of the diurnal cycle of shallow cumulus convection over land, Quarterly Journal of the Royal Meteorological Society: A journal of the atmospheric sciences, applied meteorology and physical oceanography, 128, 1075–1093, 2002.

Bryan, G. H.: Spurious convective organization in simulated squall lines owing to moist absolutely unstable layers, Monthly weather review, 133, 1978–1997, 2005.

Couvreux, F., Rio, C., Guichard, F., Lothon, M., Canut, G., Bouniol, D., and Gounou, A.: Initiation of daytime local convection in a semi-arid region analysed with high-resolution simulations and AMMA observations, Quarterly Journal of the Royal Meteorological Society, 138, 56–71, 2012.

Couvreux, F., Hourdin, F., Williamson, D., Roehrig, R., Volodina, V., Villefranque, N., Rio, C., Audouin, O., Salter, J., Bazile, E., et al.: Process-based climate model development harnessing machine learning: I. A calibration tool for parameterization improvement, Journal of Advances in Modeling Earth Systems, 13, e2020MS002 217, 2021.

Daleu, C. L., Plant, R., Woolnough, S. J., Sessions, S., Herman, M., Sobel, A., Wang, S., Kim, D., Cheng, A., Bellon, G., et al.: Intercomparison of methods of coupling between convection and large-scale circulation: 1. Comparison over uniform surface conditions, Journal of Advances in Modeling Earth Systems, 7, 1576–1601, 2015.

Del Genio, A. D., Wu, J., Wolf, A. B., Chen, Y., Yao, M.-S., and Kim, D.: Constraints on cumulus parameterization from simulations of observed MJO events, Journal of Climate, 28, 6419–6442, 2015.

Diallo, F., Hourdin, F., Rio, C., Traore, A.-K., Mellul, L., Guichard, F., and Kergoat, L.: The surface energy budget computed at the grid-scale of a climate model challenged by station data in West Africa, Journal of Advances in Modeling Earth Systems, 9, 2710–2738, 2017.

Dirmeyer, P. A., Cash, B. A., Kinter, J. L., Jung, T., Marx, L., Satoh, M., Stan, C., Tomita, H., Towers, P., Wedi, N., et al.: Simulating the diurnal cycle of rainfall in global climate models: Resolution versus parameterization, Climate dynamics, 39, 399–418, 2012.

Dorrestijn, J., Crommelin, D. T., Siebesma, A. P., and Jonker, H. J.: Stochastic parameterization of shallow cumulus convection estimated from high-resolution model data, Theoretical and Computational Fluid Dynamics, 27, 133–148, 2013.

Emanuel, K. A.: A scheme for representing cumulus convection in large-scale models, Journal of Atmospheric Sciences, 48, 2313–2329, 1991.

Feng, Z., Hagos, S., Rowe, A. K., Burleyson, C. D., Martini, M. N., and de Szoeke, S. P.: Mechanisms of convective cloud organization by cold pools over tropical warm ocean during the AMIE/DYNAMO field campaign, Journal of Advances in Modeling Earth Systems, 7, 357–381, 2015.

Gettelman, A., Truesdale, J., Bacmeister, J., Caldwell, P., Neale, R., Bogenschutz, P., and Simpson, I.: The Single Column Atmosphere Model version 6 (SCAM6): Not a scam but a tool for model evaluation and development, Journal of Advances in Modeling Earth Systems, 11, 1381–1401, 2019.

Grandpeix, J.-Y. and Lafore, J.-P.: A density current parameterization coupled with Emanuel's convection scheme. Part I: The models, Journal of the Atmospheric Sciences, 67, 881–897, 2010.

Grandpeix, J.-Y., Phillips, V., and Tailleux, R.: Improved mixing representation in Emanuel's convection scheme, Quarterly Journal of the Royal Meteorological Society: A journal of the atmospheric sciences, applied meteorology and physical oceanography, 130, 3207–3222, 2004.

Grandpeix, J.-Y., Lafore, J.-P., and Cheruy, F.: A density current parameterization coupled with Emanuel's convection scheme. Part II: 1D simulations, Journal of the Atmospheric Sciences, 67, 898–922, 2010.

Grant, L. D., Lane, T. P., and van den Heever, S. C.: The role of cold pools in tropical oceanic convective systems, Journal of the Atmospheric Sciences, 75, 2615–2634, 2018.

Guichard, F., Petch, J., Redelsperger, J.-L., Bechtold, P., Chaboureau, J.-P., Cheinet, S., Grabowski, W., Grenier, H., Jones, C., Köhler, M., et al.: Modelling the diurnal cycle of deep precipitating convection over land with cloud-resolving models and single-column models, Quarterly Journal of the Royal Meteorological Society: A journal of the atmospheric sciences, applied meteorology and physical oceanography, 130, 3139–3172, 2004.

Haerter, J. O. and Schlemmer, L.: Intensified cold pool dynamics under stronger surface heating, Geophysical Research Letters, 45, 6299–6310, 2018.

Hourdin, F., Couvreux, F., and Menut, L.: Parameterisation of the dry convective boundary layer based on a mass flux representation of thermals, Journal of the Atmospheric Sciences, 59, 1105–1123, 2002.

Hourdin, F., Musat, I., Bony, S., Braconnot, P., Codron, F., Dufresne, J.-L., Fairhead, L., Filiberti, M.-A., Friedlingstein, P., Grandpeix, J.-Y., et al.: The LMDZ4 general circulation model: climate performance and sensitivity to parametrized physics with emphasis on tropical convection, Climate Dynamics, 27, 787–813, 2006.

Hourdin, F., Foujols, M.-A., Codron, F., Guemas, V., Dufresne, J.-L., Bony, S., Denvil, S., Guez, L., Lott, F., Ghattas, J., et al.: Impact of the LMDZ atmospheric grid configuration on the climate and sensitivity of the IPSL-CM5A coupled model, Climate Dynamics, 40, 2167–2192, 2013.

Hourdin, F., Jam, A., Rio, C., Couvreux, F., Sandu, I., Lefebvre, M.-P., Brient, F., and Idelkadi, A.: Unified Parameterization of Convective Boundary Layer Transport and Clouds With the Thermal Plume Model, https://doi.org/10.1029/2019MS001666, 2019.

Hourdin, F., Rio, C., Grandpeix, J.-Y., Madeleine, J.-B., Cheruy, F., Rochetin, N., Jam, A., Musat, I., Idelkadi, A., Fairhead, L., et al.: LMDZ6A: The atmospheric component of the IPSL climate model with improved and better tuned physics, Journal of Advances in Modeling Earth Systems, 12, e2019MS001 892, 2020.

Hourdin, F., Rio, C., Jam, A., Traore, A.-K., and Musat, I.: Convective Boundary Layer Control of the Sea Surface Temperature in the Tropics, J. of Adv. in Modeling Earth Systems, 12, e01988, https://doi.org/10.1029/2019MS001988, 2020.

Hourdin, F., Williamson, D., Rio, C., Couvreux, F., Roehrig, R., Villefranque, N., Musat, I., Fairhead, L., Diallo, F. B., and Volodina, V.: Process-based climate model development harnessing machine learning: II. Model calibration from single column to global, Journal of Advances in Modeling Earth Systems, 13, e2020MS002 225, 2021.

Jam, A., Hourdin, F., Rio, C., and Couvreux, F.: Resolved Versus Parametrized Boundary-Layer Plumes. Part III: Derivation of a Statistical Scheme for Cumulus Clouds, 147, 421–441, https://doi.org/10.1007/s10546-012-9789-3, 2013.

Jeevanjee, N. and Romps, D. M.: Convective self-aggregation, cold pools, and domain size, Geophysical Research Letters, 40, 994–998, 2013.

Kendon, E. J., Roberts, N. M., Senior, C. A., and Roberts, M. J.: Realism of rainfall in a very high-resolution regional climate model, Journal of Climate, 25, 5791–5806, 2012.

Khairoutdinov, M. and Randall, D.: High-resolution simulation of shallow-to-deep convection transition over land, Journal of the atmospheric sciences, 63, 3421–3436, 2006.

Khairoutdinov, M. F. and Randall, D. A.: Cloud resolving modeling of the ARM summer 1997 IOP: Model formulation, results, uncertainties, and sensitivities, Journal of the Atmospheric Sciences, 60, 607–625, 2003.

Krueger, S. K., Morrison, H., and Fridlind, A. M.: Cloud-resolving modeling: ARM and the GCSS story, Meteorological Monographs, 57, 25–1, 2016.

Kurowski, M. J., Suselj, K., Grabowski, W. W., and Teixeira, J.: Shallow-to-deep transition of continental moist convection: Cold pools, surface fluxes, and mesoscale organization, Journal of the Atmospheric Sciences, 75, 4071–4090, 2018.

Lac, C., Chaboureau, J.-P., Masson, V., Pinty, J.-P., Tulet, P., Escobar, J., Leriche, M., Barthe, C., Aouizerats, B., Augros, C., et al.: Overview of the Meso-NH model version 5.4 and its applications, Geoscientific Model Development, 11, 1929–1969, 2018.

Lafore, J.-P. and Moncrieff, M. W.: A numerical investigation of the organization and interaction of the convective and stratiform regions of tropical squall lines, Journal of Atmospheric Sciences, 46, 521–544, 1989.

Legay, A., Deremble, B., and Burchard, H.: Derivation and implementation of a non-local term to improve the oceanic convection representation within the k–ϵ parameterization, Journal of Advances in Modeling Earth Systems, 17, e2024MS004 243, 2025.

Lochbihler, K., Lenderink, G., and Siebesma, A. P.: Cold pool dynamics shape the response of extreme rainfall events to climate change, Journal of Advances in Modeling Earth Systems, 13, e2020MS002 306, 2021.

Lothon, M., Campistron, B., Chong, M., Couvreux, F., Guichard, F., Rio, C., and Williams, E.: Life cycle of a mesoscale circular gust front observed by a C-band Doppler radar in West Africa, Monthly weather review, 139, 1370–1388, 2011.

Meyer, B. and Haerter, J. O.: Mechanical forcing of convection by cold pools: Collisions and energy scaling, Journal of Advances in Modeling Earth Systems, 12, e2020MS002 281, 2020.

Pantillon, F., Knippertz, P., Marsham, J. H., and Birch, C. E.: A parameterization of convective dust storms for models with mass-flux convection schemes, Journal of the Atmospheric Sciences, 72, 2545–2561, 2015.

Park, S.: A unified convection scheme (UNICON). Part I: Formulation, Journal of the Atmospheric Sciences, 71, 3902–3930, 2014.

Provod, M., Marsham, J., Parker, D., and Birch, C.: A characterization of cold pools in the West African Sahel, Monthly Weather Review, 144, 1923–1934, 2016.

Qian, L., Young, G. S., and Frank, W. M.: A convective wake parameterization scheme for use in general circulation models, Monthly weather review, 126, 456–469, 1998.

Randall, D., Khairoutdinov, M., Arakawa, A., and Grabowski, W.: Breaking the cloud parameterization deadlock, Bulletin of the American Meteorological Society, 84, 1547–1564, 2003.

Redelsperger, J.-L., Diedhiou, A., Flamant, C., Janicot, S., Lafore, J.-P., Lebel, T., Polcher, J., Bourlès, B., Caniaux, G., de Rosnay, P., et al.: Amma, une étude multidisciplinaire de la mousson ouest-africaine, La meteorologie, 54, 22–32, 2006.

Rio, C. and Hourdin, F.: A thermal plume model for the convective boundary layer: Representation of cumulus clouds, Journal of the atmospheric sciences, 65, 407–425, 2008.

Rio, C., Hourdin, F., Grandpeix, J.-Y., and Lafore, J.-P.: Shifting the diurnal cycle of parameterized deep convection over land, Geophysical Research Letters, 36, 2009.

Rio, C., Hourdin, F., Couvreux, F., and Jam, A.: Resolved versus parametrized boundary-layer plumes. Part II: continuous formulations of mixing rates for mass-flux schemes, Boundary-layer meteorology, 135, 469–483, 2010.

Rio, C., Grandpeix, J.-Y., Hourdin, F., Guichard, F., Couvreux, F., Lafore, J.-P., Fridlind, A., Mrowiec, A., Roehrig, R., Rochetin, N., et al.: Control of deep convection by sub-cloud lifting processes: the ALP closure in the LMDZ5B general circulation model, Climate dynamics, 40, 2271–2292, 2013.

Rochetin, N., Grandpeix, J.-Y., Rio, C., and Couvreux, F.: Deep convection triggering by boundary layer thermals. Part II: Stochastic triggering parameterization for the LMDZ GCM, Journal of the Atmospheric Sciences, 71, 515–538, 2014.

Rochetin, N., Hohenegger, C., Touzé-Peiffer, L., and Villefranque, N.: A physically based definition of convectively generated density currents: Detection and characterization in convection-permitting simulations, Journal of Advances in Modeling Earth Systems, 13, e2020MS002 402, 2021.

Rotunno, R., Klemp, J. B., and Weisman, M. L.: A theory for strong, long-lived squall lines, Journal of Atmospheric Sciences, 45, 463–485, 1988.

Sadourny, R.: January and July performances of the LMD general circulation model, New perspectives in climate modeling, 1984.

Siebesma, A. P., Bretherton, C. S., Brown, A., Chlond, A., Cuxart, J., Duynkerke, P. G., Jiang, H., Khairoutdinov, M., Lewellen, D., Moeng, C.-H., et al.: A large eddy simulation intercomparison study of shallow cumulus convection, Journal of the Atmospheric Sciences, 60, 1201–1219, 2003.

Stephens, G. L., L'Ecuyer, T., Forbes, R., Gettelmen, A., Golaz, J.-C., Bodas-Salcedo, A., Suzuki, K., Gabriel, P., and Haynes, J.: Dreary state of precipitation in global models, Journal of Geophysical Research: Atmospheres, 115, 2010.

Strauss, C., Ricard, D., Lac, C., and Verrelle, A.: Evaluation of turbulence parametrizations in convective clouds and their environment based on a large-eddy simulation, Quarterly Journal of the Royal Meteorological Society, 145, 3195–3217, 2019.

Tan, J., Oreopoulos, L., Jakob, C., and Jin, D.: Evaluating rainfall errors in global climate models through cloud regimes, Climate Dynamics, 50, 3301–3314, 2018.

Torri, G. and Kuang, Z.: On cold pool collisions in tropical boundary layers, Geophysical Research Letters, 46, 399–407, 2019.

Touzé-Peiffer, L., Vogel, R., and Rochetin, N.: Cold pools observed during eurec 4 a: Detection and characterization from atmospheric soundings, Journal of Applied Meteorology and Climatology, 61, 593–610, 2022.

Vogel, R., Konow, H., Schulz, H., and Zuidema, P.: A climatology of trade-wind cumulus cold pools and their link to mesoscale cloud organization, Atmospheric Chemistry and Physics, 21, 16 609–16 630, 2021.

Weisman, M. L. and Rotunno, R.: "A theory for strong long-lived squall lines" revisited, Journal of the Atmospheric Sciences, 61, 361–382, 2004.

Williamson, D., Goldstein, M., Allison, L., Blaker, A., Challenor, P., Jackson, L., and Yamazaki, K.: History matching for exploring and reducing climate model parameter space using observations and a large perturbed physics ensemble, Climate dynamics, 41, 1703–1729, 2013.

Yamada, T.: Simulations of Nocturnal Drainage Flows by a q^2l Turbulence Closure Model, J. Atmos. Sci., 40, 91–106, 1983.

Young, G. S., Perugini, S. M., and Fairall, C.: Convective wakes in the equatorial western Pacific during TOGA, Monthly Weather Review, 123, 110–123, 1995.

Zhang, M., Somerville, R. C., and Xie, S.: The SCM concept and creation of ARM forcing datasets, Meteorological Monographs, 57, 24–1, 2016.

Zuidema, P., Torri, G., Muller, C., and Chandra, A.: A survey of precipitation-induced atmospheric cold pools over oceans and their interactions with the larger-scale environment, Surveys in Geophysics, 38, 1283–1305, 2017.